MECHANICAL BEHAVIOR AND MICROSTRUCTURE OF SELF-ASSEMBLING OLIGOPEPTIDE GELS

by

Nathan Allen Hammond

B.S. Mechanical and Aerospace Engineering
Utah State University, 2003

M.S. Biomedical Engineering
Purdue University, 2005

SUBMITTED TO THE DEPARTMENT OF MECHANICAL ENGINEERING IN PARTIAL FULFILLMENT OF THE REQUIREMENTS FOR THE DEGREE OF

DOCTOR OF PHILOSOPHY IN MECHANICAL ENGINEERING
AT THE
MASSACHUSETTS INSTITUTE OF TECHNOLOGY

SEPTEMBER 2010

Signature of Author: _____

Department of Mechanical Engineering
July 2, 2010

Certified by: _____

Roger D. Kamm
Germeshausen Professor of Mechanical and Biological Engineering
Thesis Supervisor

Accepted by: _____

David E. Hardt
Chairman, Department Committee on Graduate Students

Mechanical Behavior and Microstructure of Self-Assembling Oligopeptide Gels

by

Nathan A. Hammond

Submitted to the Department of Mechanical Engineering
on August 6, 2010 in Partial Fulfillment of the
Requirements for the Degree of Doctor of Philosophy in
Mechanical Engineering

Abstract

Hydrogels have become widely used in the fields of tissue engineering and drug delivery. One class of hydrogel is formed from synthetic oligopeptides that self-assemble into a solution of beta-sheet filaments. These filaments can aggregate to form a gel suitable for culture of various cell types. Examples of such self-assembling peptides are RAD16-I, RAD16-II, and KLD-12.

One limitation of self-assembling peptide hydrogels is their mechanical weakness. Herein are presented computational and experimental studies that elucidate the microstructure and mechanical behavior of these materials. Strategies to enhance their mechanical properties are also examined.

Steered molecular dynamics modeling was used to characterize the mechanical interaction between filaments, and a coarse-grained model was developed to extend the system to ordinary time scales. A microindentation assay was developed and used to characterize the mechanical properties of gels. Several strategies for enhancing the gels' mechanical properties were tested. Gel microstructure was observed in thin sections of material with transmission electron microscopy, revealing in detail the loose, disorganized structure of assembled beta-sheet filaments.

The results demonstrate that these self-assembling peptide gels are formed from a loosely arranged structure of beta-sheet filaments, not from dense bundles of parallel filaments as was previously proposed. Estimates of gel stiffness based on this loose structure are in approximate agreement with experimental measurements. Among the strategies tested to increase gel stiffness, introducing cross-links and increasing solid concentration proved to be effective approaches.

Thesis Supervisor: Roger D. Kamm
Title: Germeshausen Professor of Mechanical and Biological Engineering

Acknowledgments

Foremost, I want to thank Professor Roger Kamm, my advisor for the last five years, and one of my role models professionally and personally. I don't know anyone more precise in thought or more kind in nature than Roger. It is hard to overstate what a towering influence an advisor has in the lives of his or her students. For half a decade, my work, my studies, my ambitions, and my identity have been wrapped up in the Kamm lab, and I can only be proud of that fact. I think I will look back on my years at MIT as a very positive time, and the thanks for this goes largely to Professor Kamm. After I've moved on to the next chapter, I look forward to dropping by once in a while for a run along the Charles.

I also want to acknowledge and thank three other great role models, my committee members. For Professor Shuguang Zhang, I have come to admire his energy, his passion for research, and his visionary style that goes straight to the problems that matter. For Professor Markus Buehler, I would be ten times as effective as I am if I could emulate his professional focus and his work ethic, and it has been a pure pleasure to work with him for the last few years. For Professor Alan Grodzinsky, just his presence in the room brings the air to life, and if I ever have the privilege of teaching, I want to be just exactly like him.

I never really planned on going to MIT, and I never really planned to get a PhD. There is a long list of overworked underpaid miracle doers who shaped my educational path a lot more actively than I did, and I want to give them my profound thanks. I will mention a few specifically. Thanks to my first grade teacher Eloise McBride, who took time every day to think up activities that would challenge me. She always drew up the seating chart to put this whisperingly shy, mop-haired boy next to one of the cute, sweet girls in class because, as she told me 23 years later, "I wanted you to experience the good things in life." Thanks to the queen of creativity Aartje Crumley, maker of stretchy minds. Snake River School District lost its best warrior in the fight against boredom when she retired. Thanks to Coach Ed Jackson, who made me memorize *Invictus*, trained me to spell all the days of the week in under five seconds, and introduced me to the joy of running. Thanks to Elaine Asmus, a hero of mine, for opening my eyes to the wonders of biology and infusing the world of education with passion. Thanks to James Odell for making the English language such a noble and mysterious thing. Thanks to Professor Lance Littlejohn for engaging my mind in differential equations, and for looking me in the eye and telling me with conviction that I should get a Ph.D. Thanks to the other faculty at Utah State who were just so damn smart and on top of it that you had to love what they said in class: Clair Batty, Thomas Blotter, Thomas Fronk, Robert Spall, and others. Thanks to Sherry Harbin at Purdue for getting me excited about tissue engineering from our first conversation, and for inducting me into the amazing world of scientific research. To all of them, my warm, sincere thanks.

I want to thank and acknowledge my family for their support. I am immensely thankful to my Mom and Dad, who have only become closer friends to me since I left the West seven years ago. I'm thankful to my five weird, weird siblings, who are my best and

most lasting friends and also a kind of funhouse mirror reflection of myself. I'm so grateful to Dave and Kim and my beautiful nieces and handsome nephew who joined me on the East Coast and made Boston feel so much more like home. Thanking my family in my little thesis feels like waving hello to the sun. They are my roots, my core, and their presence in my life is totally immovable.

More directly tied to my Ph.D. work, and oh so dear to my heart, I have a second family to thank as well. Idaho is just too far away, and you can't live without family, so I want to acknowledge the impromptu family that has grown around me in Cambridge. These are my lab mates, my roommates, and my friends, who make up the living fabric of every day.

And how could I have gotten through MIT without Cherry and Anusuya?! We started in lab at about the same time, and like family they were just unavoidably there every day. So mostly by accident we eventually saw each other through so many ups and downs and life crises and leaky ruined experiments and abstract arguments and mid-afternoon coffee breaks and adventures and recalibrations of life trajectory that in the end I feel as if we grew up together and they are my sisters.

Table of Contents

Chapter 1 Introduction and background

1.1 Hydrogels

With ever increasing attention in the fields of tissue engineering and drug delivery systems, hydrogels have become very prominent in biomaterials research. Gels are colloids in which a fluid phase is dispersed through a solid phase. The solid phase is often dilute, and fluid can constitute more than 99% of the gel mass. Still, due to the continuity of the solid phase, gels exhibit no flow at steady state [1]. The term "hydrogel" applies when the fluid phase is aqueous.

Given their particular combination of solid and fluid properties, hydrogels are ideally suited for applications that require the transport of material or the migration of cells through a solid framework. The need for materials with these properties makes hydrogels almost ubiquitous for 3-dimensional cell culture and tissue engineering [2]. Another established use is in drug delivery systems where active molecules are incorporated into a hydrogel to be gradually released [3]. Sophisticated delivery systems have utilized hydrogels engineered to release a payload in response to an environmental cue such as pH, temperature, or the concentration of a specific molecule [4]. A diagram of a "smart" hydrogel that swells in the presence of glucose [5] is shown in Figure 1.1.

1.1.1 The mechanical properties of hydrogels

Note that within our definition of hydrogel—a colloid with aqueous fluid dispersed in a continuous solid phase—there is a wide range of possible microstructures. The structure of the solid phase in a given gel is integral to that gel's mechanical behavior.

The first hydrogels studied for modern medical applications were made by cross-linking solutions of flexible hydrophilic synthetic polymers [6]. Analysis of the mechanical behavior of these polymer networks typically considers hydrostatic pressure

arising from the polymers' hydrophilicity, tension in the polymer chains, and the extent of condensation of the polymer (e.g. [7, 8]). In these gels, distinction has been made between those in which polymers remain at their equilibrium length after cross-linking and those which are allowed to swell [1]. Flexible polymers behave as entropic (Gaussian) springs and may be described by the freely jointed chain model [9]. Before polymers are fully extended and experience backbone stretch, tension arises from the decreased entropy associated with the reduced number of conformations available to a polymer as it is extended. Many biologically derived hydrogels are made of flexible polymers and behave similarly to the synthetic polymers described above. These include polysaccharides (starch, cellulose, chitin, glycosaminoglycans), denatured proteins (gelatin) and nucleic acids.

Other gels can be well described by the cellular solids paradigm explained by Gibson and Ashby [10]. This model applies if the microstructural components of the solid phase are not only resistant to tension but to shear, bending, and compression as well. The mechanical behavior of one unit cell may be evaluated, and the results scaled to describe the bulk material behavior. For example, gels have been made by filling the space between packed microbeads with cross-linked PEG or gelatin before dissolving the bead material and refilling the void spaces with buffered saline solution [11].

Gels made from a network of semi-rigid polymers (usually elongate structural proteins such as actin) are well described by the biopolymers model introduced by MacKintosh et al. [12]. This model has two different forms to account for densely cross-linked gels (in which the characteristic cross-link spacing is equal to the mesh size) or

gels that are not densely linked (in which the entanglement length is taken to be the distance at which typical bending deflections of a fiber are equal to the mesh size).

In any of these hydrogels other confounding effects may be present. If the pore size is sufficiently small and the length scale of the bulk material sufficiently large, resistance to flow can give rise to time-dependent effects associated with poroelasticity [13]. Time-dependent effects may also arise due to viscoelasticity of the solid phase [14]. The exchange of ions between a charged hydrogel and the surrounding fluid may also give rise to complex time-dependent mechanical effects [15], described for example by the triphasic model of Mow et al. [16]. Other mechanical behaviors arise in connection with special material properties, for example shear thinning and recovery in materials with hydrophobic moieties whose bonds can rupture and reform [17] or mechanical responses to environmental stimuli such as temperature or pH [4].

Since diffusion and cell migration are often critical to a hydrogel's function, gels are often designed with small dimensions and a dilute solid phase. They therefore tend to be mechanically weak, and attention should be given to a gel's mechanical properties as an important component of design. A number of strategies have been employed to increase gel strength while maintaining a low solid fraction. For example, covalent cross-linking of protein-based gels such as collagen can increase stiffness and strength [18]. Other innovative approaches have been developed such as the use of figure-eight-shaped sliding cross-links to distribute loads more equitably across a synthetic polymer network [19] or generating two independent solid networks that act in parallel [20].

In summary, while all hydrogels exhibit some solid properties due to their continuous solid phase, the exact nature of their mechanical behavior may be complex and depends on the microstructure of a particular gel.

1.2 Gels made with self-assembling oligopeptides that form ß-sheet (amyloid) filaments

In studying the DNA-binding yeast protein zuotin, Zhang et al. [21] noted that it contains a 34-residue sequence of alternating hydrophobic and hydrophilic residues, including the 16-residue sequence $[EAEAKAKA]_2$. The hydrophilic residues in this sequence have a self-complementary pattern of charge (- - + + - - + +). A synthesized peptide of this sequence, commonly called EAK16, was found to readily adopt a ß-sheet conformation and assemble into macroscopic gels [22].

Following this discovery, a series of new synthetic peptides demonstrated the robust tendency of the alternating charge motif in EAK16 to form gels, even when substitutions are made with similar residues (e.g. $[RARADADA]_2$) [23]. More or less frequent repeats also form gels (e.g. $[RADA]_4$ and RARARARADADADADA) [23], as do sequences of varied length (e.g. $[FEFK]_3$) [24].

Circular dichroism and Congo red staining both indicate that these peptides assemble into a ß-sheet structure [24-26]. Self-assembling peptides that have been imaged by atomic force microscopy exhibit long filaments with a helical structure (KFE8 [27]) or a straight ribbon-like structure the thickness of two stacked ß-sheets (e.g. RAD16-I [28]).

Synthetic peptides that assemble into ß-sheets have been known for many years and were studied in the context of pathogenic amyloids or fundamental protein physics [29-31]. However, in the past two decades since Zhang's discovery of EAK16 a number

of researchers have begun to develop self-assembling ß-sheet-forming peptide gels for engineering applications [32-34].

1.2.1 Self-assembly of peptides into ß-sheet filaments and gels

Early on in the study of self-assembling peptides, it was noted that gel formation is a two-stage process. EAK16 forms ß-sheet structures that are stable over a wide range of pH, temperature, and concentration of denaturing agents (SDS, guanidine and HCl, or Urea); a separate assembly process occurs to form macroscopic structures with the addition of salt [35].

Models for assembly of filaments often explain interfilament assembly behavior in terms of an energy balance to minimize free energy. In the model of Aggeli et al. [36], filaments stack together in dense bundles whose size is determined by an energetic trade-off, the benefit of filaments binding versus the expense incurred by the partial untwisting of their helical structure as they bind. Caplan et al. [37] assert that assembly is well described by DLVO (Derjaguin, Landau, Verwey, and Overbeek) theory, which balances van der Waals attraction with energy of interaction between the layers of counterions near the charged surfaces.

However, much remains unknown about the structure of filaments associating to form a gel. It may be that the assembled structure does not represent the global minimum of free energy, but rather a structure that is kinetically trapped. This phenomenon has been demonstrated in actin filaments in the presence of fascin, an actin binding protein that promotes parallel bundling. When monomeric actin is allowed to assemble in the presence of fascin, well ordered, parallel bundles form. When filamentous actin is mixed with fascin, however, entanglement prevents such an ordered structure from forming [38]. This represents a state that is kinetically trapped and not the global energetic minimum.

1.2.2 Mechanical properties of self-assembling peptide gels

Table 1.1 summarizes data from a number of studies providing storage moduli or Young's moduli of self-assembling peptide gels, and failure strength where available. Mechanical measurements of collagen I gel are also presented for comparison.

Caplan et al. demonstrated that a large difference in elastic modulus may result from variations in the peptide sequence [39]. Nevertheless, even the stiffest self-assembling peptide (RAD16-II) in Table 1.1 has a storage modulus of just 756 Pa at 0.3% [40], compared to a Young's modulus of 24.3 kPa for collagen I at the same concentration [41]. (For collagen, this is the maximum slope of the stress-strain curve, as shown in Figure 1.2A). The failure strength of peptide gels is also lower. A 0.33% EFK8 gel fails at 120-220 Pa in tension [42], while 0.3% collagen fails at 10 kPa [41].

An important difference between self-assembling peptide and collagen gel behavior is seen in the shape of the stress-strain curves in Figure 1.2. Collagen has a significant "toe region" before it reaches its maximum Young's modulus, allowing typical failure strains of 50-60% [41]. Self-assembling peptide gels, however, exhibit brittle behavior with linear stress-strain curves and failure at strains of just a few percent [42] .

1.2.3 Microstructure of self-assembling peptide gels

While the structure of individual filaments of self-assembling peptide is relatively well understood, much remains unknown about the structure of assembled filaments in aqueous solution. Clearly this structure is an important determinant of bulk mechanical properties. Attention is given to this question throughout this work, and a review of imaging techniques and images of peptide gel microstructure is included in the appendix.

1.2.4 Self-assembling peptides as a simple system for protein design

In many ways self-assembling peptides present exciting opportunities for material design. While designing proteins of biological complexity still remains largely beyond the ability of researchers, β-sheet-forming peptides are simple enough to allow *de novo* design. They are short enough to be synthesized at relatively low expense. They may be decorated in a number of ways: adding short binding motifs directly during peptide synthesis [28]; synthesizing biotinylated peptide for the attachment of larger biotinylated proteins via streptavidin [43]; or by enzyme-mediated covalent binding with other short peptides [44].

A striking example of peptide design with these materials comes from Joel Schneider, Darrin Pochan et al. [34]. They created a 20-amino acid peptide with a hairpin turn in the center that folds only in basic conditions, making pH a trigger for self-assembly into ß-sheet filaments. Replacing one residue with a photosensitive caged compound, they later made a peptide whose assembly is triggered by light [45].

1.3 Mechanical testing of gels

Some consideration should be given to the methods for mechanical testing of gels. Biological materials are often very costly and may be available only in small volumes. Using rheometers and tensile testing machines that are designed for relatively large sample volumes, mechanical testing can be prohibitively expensive, particularly for failure testing where many repetitions are needed and for high-concentration materials.

A review of the mechanical testing methods used on self-assembling peptide gels shown in Table 1.1 reveals that bulk measurement techniques routinely require more than 200 µl per sample. The most common method is cone-and-plate or parallel plate rheometry for measurement of storage and loss moduli with no measurement of failure

properties [32-34, 39, 40, 46, 47]. Forming gels on the rheometer plate may require as much as 15 hours of machine time per sample [39]. An alternative is forming the gels elsewhere before transferring them to the rheometer [40], but this risks damaging the fragile specimens and presents difficulties in consistently matching the gap distance to the material thickness.

Tensile testing of cast specimens has been performed for collagen gels [41], using 1 ml of gel for each failure test. The tensile testing method used by Leon et al. stands out for the small volume of material used per test (4 μl) while measuring elastic and failure properties. In this method peptide gel emerging from a needle is brought into adhesive contact with an analytical scale, then extruded while the needle retracts from the surface. The extrusion is halted while the needle retracts farther, stretching and breaking the thread of gel. Visual data is obtained with a CCD camera to measure lateral deformation while force data is read from the scale during displacement at a controlled rate. While this method has many attractive features, it requires a custom-made apparatus with cumbersome operation (including manually recording of values from the analytical balance during loading).

Microindentation provides an attractive alternative to these methods. In recent years nano- and microindentation have been used for mechanical characterization of gels [46], thin films [47], tissue specimens [48], and individual cells [49]. In some cases indentation has been used to measure not only elastic properties but also poroelasticity [13], and plastic failure [50].

1.4 Thesis overview

In this work, the overarching goal is to better understand the mechanical behavior of self-assembling peptide gels, and to explore methods for making materials that

combine the many advantages of self-assembling peptides and substantially higher strength.

Chapter 2 examines the mechanical interactions between filaments using computational techniques. CHARMM molecular dynamics software is used to analyze all-atom representations of filament segments under shear loads. A coarse-grained model is presented that quantitatively captures the behavior observed in the all-atom model. The results help to illustrate the fundamental behavior of slippage between filaments formed from periodic structures and aligned in parallel, and also help to rule out some possible descriptions of the microstructure of self-assembling peptide gels.

Chapter 3 presents the development of a micro-indentation assay for mechanical characterization of gels. The effect of concentration on gel stiffness is reconfirmed, and two new strategies for improving the mechanical properties of peptide gels are proposed and tested: glutaraldehyde cross-linking of peptide side chains, and varying the length of filaments from which gels are formed.

In Chapter 4 some of the results from two collaborations are presented, with the mechanical characterization of self-assembling peptide gels specially designed for tissue engineering applications.

Concluding comments are included in Chapter 5.

Table 1.1
Mechanical properties of various self-assembling peptide gels and collagen I gel

Study	*Material*	*Sequence*	*wt%*	*Bath*	*Method*	*G' (Pa)*
Caplan et al. 2002 [39]	KFE8	$[FKFE]_2$	1.0	PBS pH 7.4	Rheometry 0.1 rad/s	410±280
	KFE12	$[FKFE]_3$				2300±740
	KFE16	$[FKFE]_4$				170±110
	KIE12	$[IKIE]_3$				2200±510
	KVE12	$[VKVE]_3$				2900±710
	KFQ12	$[FKFQ]_3$				3500±910
Aggeli et al. 1997 [32]	K24	KLEALWV-LGFFGFFT-LGIMLSW	2.5	2-chloroethanol	Rheometry 1-10 rad/s	330
Schneider et al. 2002 [34]	MAX1	$VKVKVKVKV^{D}P$-PTKVKVKVKV	2.0	1:1 with 250 mM borate/ 20 mM NaCl pH 9.0	Rheometry 0.1-100 rad/s	~1600
Sieminski et al. 2007 [40]	RAD16-I	$[RADA]_4$	0.1	PBS	Rheometry 0.1-1 rad/s	44±31
			0.15			109±23
			0.2			225±99
			0.25			319±90
			0.3			536±143
			0.5			1320±548
			1.0			4900±1970
	RAD16-II	$[RARADADA]_2$	0.1			45±38
			0.15			189±49
			0.2			388±274
			0.25			681±153
			0.3			756±186
			0.5			2250±435
			1.0			11900±1900
Study	*Material*	*Sequence*	*wt%*	*Bath*	*Method*	*E (Pa)/ $\sigma_{failure}$ (Pa)*
Leon et al. 1998 [42]	EFK8	$[KFEF]_2$	0.27	Salt solution	Uniaxial tensile test	1590 / 50.5
			0.33			2900 / 176
			0.54			6320 / 123
			1.0			14700 / 197
Roeder et al. 2002 [41]	Collagen I		0.03	PBS pH 7.4	Uniaxial tensile test	1540±507 / 708±79
			0.1			10700±1930 / 583±55
			0.2			16600±2680 / 592±53
			0.3			24300±4160 / 605±50

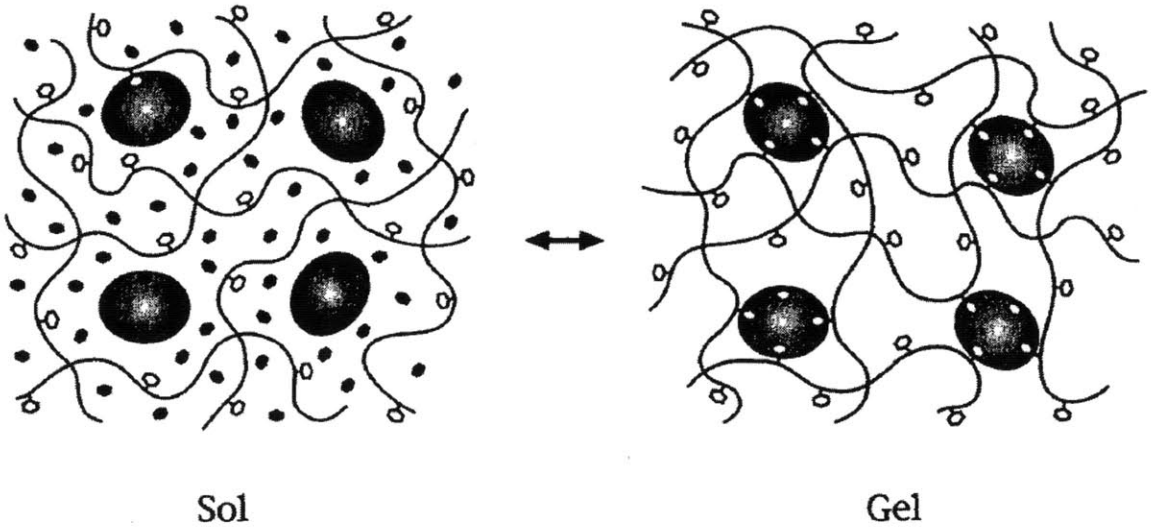

Figure 1.1. A cartoon representation of a "smart" gel that softens or converts to a sol in the presence of glucose. Vinylpyrrolidinone polymers are covalently conjugated to glucose, which is bound by the protein concanavalin A. In the presence of dissolved glucose, competitive binding frees the bonds between concavalin A and the polymers. (Image from Lee and Park [5].)

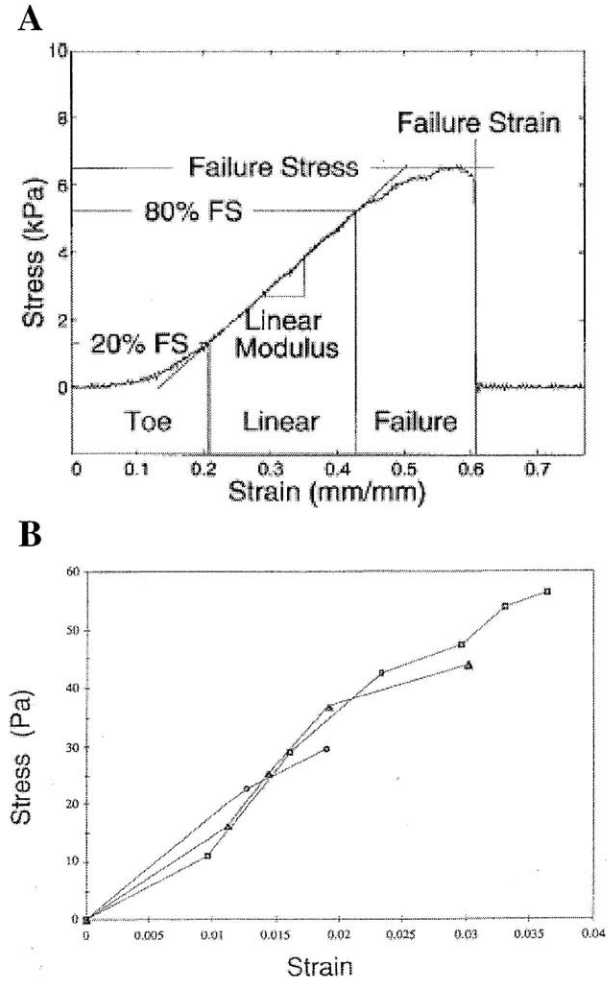

Figure 1.2. Typical stress-strain curves for uniaxial tensile testing of (A) collagen (0.2%), from Roeder et al. [41], and (B) the self-assembling peptide EFK8 (0.27%), from Leon et al. [42].

Chapter 2 Elastic deformation and failure in protein filament bundles: atomistic simulations and coarse-grained modeling*

The synthetic peptide RAD16-II has shown promise in tissue engineering and drug delivery. It has been studied as a vehicle for cell delivery and controlled release of IGF-1 to repair infarcted cardiac tissue, and as a scaffold to promote capillary formation for an *in vitro* model of angiogenesis. The structure of RAD16-II is hierarchical, with monomers forming long ß-sheets that pair together to form filaments; filaments form bundles approximately 30-60 nm in diameter; branching networks of filament bundles form macroscopic gels. We investigate the mechanics of shearing between the two ß-sheets constituting one filament, and between cohered filaments of RAD16-II. This shear loading is found in filament bundle bending or in tensile loading of fibers comprised of partial-length filaments. Molecular dynamics simulations show that time to failure is a stochastic function of applied shear stress, and that for a given loading time behavior is elastic for sufficiently small shear loads. We propose a coarse-grained model based on Langevin dynamics that matches molecular dynamics results and facilities extending simulations in space and time. The model treats a filament as an elastic string of particles, each having potential energy that is a periodic function of its position relative to the neighboring filament. With insight from these simulations, we discuss strategies for strengthening RAD16-II and similar materials.

2.1 Introduction

The mechanical properties of bundled filamentous proteins confer unique functionality to many important materials in biology and engineering. Filament bundles enable the extraordinary toughness of collagen [51], the frequency-selective transduction

* Material in this chapter was originally published in Biomaterials in July 2008, volume 29, issue 21, pages 3152-3160.

of sound waves by stereocilia [52], and the extension of filopodia by a migrating cell [53]. In all of these cases the fibers serve a structural role, and their mechanical properties are of great importance. Scaffold materials used as three-dimensional substrates for tissue engineering frequently have a similar structure. The scaffold's stiffness influences cell viability, migration, and differentiation, and the ability to modulate mechanical properties is therefore highly desirable. One important determinant of the properties of a filament bundle is the shear response between adjacent filaments, which may be modeled as elastic [54] or inelastic [51]. The elastic models often used for filaments are appropriate for filament bundles when energy loss due to interfilament slippage is negligible.

We introduce the term "amyloid-forming peptides" (AFP's, for brevity) to describe one class of materials that form filament bundles. Many synthetic AFP's now exist, some that copy or mimic a segment of a natural protein [22, 32, 55] and some that do not [44, 56]. Their key characteristic is the formation of filaments with a cross-ß structure, wherein monomers are aligned normal to the filament axis in either parallel [57] or antiparallel [58] fashion.

Many AFP's reviewed by Zhang [24] possess a self-complementary pattern of charged residues wherein (1) the juxtaposition of oppositely charged side chains energetically favors the formation of ß-sheets, and (2) the primary sequence alternates between hydrophobic and hydrophilic residues, resulting in a ß-sheet with one side composed of hydrophobic side chains and the other of ionizable side chains. In the present study we examine the self-complementary peptide Ac-$[RARADADA]_2$-Am, called RAD16-II. RAD16-II forms a tape-like filament of two ß-sheets with a hydrophobic core (Figure 2.1). Each ß-sheet has a hydrophobic surface of alanine side

chains while charged arginine and aspartic acid side chains form the opposing hydrophilic surface. An antiparallel ß-sheet is thought to be favored, as it has a lower energy than a parallel formation, which would juxtapose like charges [59]. At concentrations on the order of 0.1%, RAD16-II forms a macroscopic gel. These gels are networks of filament bundles 30-40 nm in diameter [40], or 10-20 nm when dehydrated [60], each large enough to include many individual filaments.

Self-assembly of individual filaments into fibers and gels is initiated when repulsive charges are either neutralized by changing pH or shielded by increasing ionic strength. The forces driving various AFP's assembly into stable gels have been attributed to salt bridges between charged residues [35], interaction of hydrophobic residues [35, 61, 62], polar organization due to amphiphilicity [63], and hydrogen bonding between glutamine residues [36]. One or more of these mechanisms may be at work in any given peptide. The fibrillar ß-sheet structure tends to make these materials tolerant to extremes of temperature and pH [35], resistant to enzymatic activity [35, 44], and congophilic [22]. Many have noted the structural similarity of synthetic amyloid-forming peptides to naturally occurring A-ß protein [22, 62], pathogenic polyglutamines [44], and silk fibroin [35], all proteins of extraordinary stability.

RAD16-II and other self-complimentary AFP's show promise for applications in tissue engineering and drug delivery. For cardiac repair, injectable RAD16-II has been proposed as a vehicle for cell delivery and a scaffold for controlled release of tethered IGF-1 [43, 64]. RAD16-II also provides a model for studying angiogenesis, as human microvascular endothelial cells embedded in RAD16-II gels give rise to a 3-D capillary-like network *in vitro* [65]. Other self-complementary AFP's used in tissue engineering

research include RAD16-I (Ac-[RADA]$_4$-Am) [66] and KLD12 (Ac-[KLDL]$_3$-Am) [26, 67].

For some applications the utility of RAD16-II and similar materials may be restricted by their low stiffness or their tendency to fracture at relatively small strains. Gel stiffness may be increased over a certain range by raising peptide concentration, but this approach is limited by peptide solubility. Some previous attempts have been made to increase the stiffness of various AFP gels. Introducing cross-links (biotin-streptavidin [68], or lysine-glutamine [44]) does not increase mechanical integrity appreciably, but materials of varied primary structure do exhibit a wide range (170-3500 Pa) of stiffness [39]. These observations suggest that the stiffness of AFP gels is not limited primarily by slippage between filament bundles, which cross-linking should restrict, but by the stiffness of the filament bundles themselves. While ß-sheet filaments have a high elastic modulus on the order of 10 GPa in tension [59], filament bundles may have little resistance to bending if slipping occurs between filaments. Such slippage reportedly occurs in bundles of carbon nanotubes [69], but this phenomenon had not yet been postulated for bundled amyloid filaments such as RAD16-II.

In this study we use simulations to probe the mechanical properties of RAD16-II filaments and inter-filament bonds. RAD16-II is selected for its simple, straight filament structure and its promise as a biomaterial. We perform molecular dynamics (MD) simulations on all-atom representations of one- and two-filament segments to observe the mechanics of elastic strain and slippage between β-sheets. Computational expense limits MD simulations to nanoseconds of duration and nanometers of filament length, therefore

we introduce a coarse-grained model of inter-filament shear to interpret and extend the MD results.

2.2 Molecular dynamics simulations

2.2.1 Methods

CHARMM version 32b was used to conduct all-atom MD simulations of the synthetic peptide Ac-[RARADADA]$_2$-Am. The CHARMM version 27 force field [70] was used to calculate the force acting on each atom, and the classical equations of motion were numerically integrated over discrete time steps to obtain trajectories. A cutoff of 16 Å was applied to nonbonded electrostatic interactions. The Nose-Hoover thermostat [71] was used to allow sampling from the canonical ensemble, and the GBSW implicit solvent model [72] was used to approximate energetic effects of water. GBSW has been shown to agree well with Poisson-Boltzmann solvers [73] and with experimental observables [74].

While it has not been experimentally determined whether RAD16-II ß-sheets have parallel or antiparallel alignment, previous simulations have shown that the antiparallel structure has significantly lower energy [59]. To make antiparallel ß-sheets, we assigned dihedral angles consistent with a ß-sheet to the peptide backbone, and positioned one peptide every 4.8 Å. A double-layer filament was created by positioning two such ß-sheets with their hydrophobic surfaces in contact. A two-filament (two double-layers) structure was created by duplicating this filament and positioning it beside the original, with the charged surfaces in contact. Each system was minimized with 200 steps of the steepest descent algorithm followed by 2000 steps of adopted basis Newton-Raphson and equilibrated at 300 °C for 500 ps. The final coordinates and velocities of the equilibrated structures were used as starting conditions for simulations. When simulations were

performed in triplicate, a second and third set of initial conditions were generated by equilibrating for a further 50 ps and 100 ps.

Shear between surfaces was created by applying to each α-carbon in one ß-sheet a constant force along the filament axis, and applying an opposite force to the α-carbons of another sheet (Figure 2.2). Because the moment from these forces would give rise to a rotation, a small force normal to the filament axis was applied to the α-carbons of the first and last two peptides of each loaded ß-sheet, such that the net moment was zero. In double-filament simulations the shear force is applied to the two outer ß-sheets while the two inner ß-sheets are not subjected to any external force, such that all three bonding surfaces are stressed (Figure 2.2B). Displacement between the backbones of two ß-sheets was calculated as the difference in mean position of the α-carbon atoms of each. Displacement was converted to shear strain by dividing by 17.5 Å, the width of one period in equilibrated, stacked filaments.

2.2.2 Linear elastic behavior

When varied levels of shear stress were applied to two stacked filaments (Figure 2.2B), a linear elastic regime with a shear modulus of 1.8 GPa (Figures 2.3, 2.4) was evident for shear stresses below 83 MPa and engineering shear strains less than about 5%. At these low levels of stress, strain was elastically recovered within a few picoseconds after the shear stress was removed. Strain softening was observed for shear loads of 125 to 208 MPa, with near-complete elastic recovery after the load was removed. At the higher end of this range, trajectories showed a slight drift following the initial abrupt change in displacement, suggesting that failure may still occur at these stresses if simulation times were extended. When these levels of shear load were removed, an initial abrupt strain recovery was followed by a drift toward zero displacement.

2.2.3 Atomistic description of shear failure

With a load of 250 MPa, the two hydrophobic surfaces in the stacked filament pair failed during the 40-ps interval (Figure 2.3), while the charged surface did not slip. To understand the nature of this failure, note in Figure 2.1 the makeup of the hydrophobic surface. The methyl side chains of alanine residues, shown in white, form a regular rectangular array. Alanine side chains from the opposite ß-sheet fill the interstices of this array to make a regular pattern with each side chain occupying a space corresponding to a minimum of free energy. In order for slippage to occur between the two ß-sheets, each methyl group must jump from one open space into the next.

Figure 2.5 shows the trajectory of one of these methyl groups relative to nearby atoms on the opposing surface. The side chain moved in discrete jumps of about 5 Å, corresponding to the spacing between ß-strands. By choosing a threshold position and measuring the time at which it is crossed by each side chain, we could discern the pattern of failure initiation and propagation on the hydrophobic intrafilament surface (Figure 2.6). In this simulation, failure began near the center of the right edge and propagated laterally along a ß-strand and longitudinally to neighboring ß-strands.

2.2.4 Time to failure

The simulation results discussed in the previous section suggest that in bundles of RAD16-II filaments, the hydrophobic surfaces are weaker than hydrophilic surfaces. This is subject to the caveat that our modeled filaments are well aligned with bound surfaces in full contact and no incorporated water molecules, while the actual geometry may be somewhat more complicated. Based on the results above we turn our attention to the apparently weaker hydrophobic surfaces by applying a shear load as demonstrated in Figure 2.2A.

Over a 1-ns window of simulation time, we observed failure of the hydrophobic surface for shear loads ≥ 200 MPa (Figure 2.7). The mean time at which slippage occurs decreased with increasing shear stress. In all three simulations at 183 MPa, failure did not occur within 1 ns. On a node of 8 CPUs, simulations have a rate of about 20 ps of per hour.

2.4 Coarse-grained model of filament slippage

While longer filaments and longer MD simulation times would help to illuminate the behavior of RAD16-II filaments, the computational expense quickly becomes prohibitive. To gain insights into these computationally expensive regimes of material behavior, we developed a coarse-grained model of filament slippage.

2.4.1 The model

Here we introduce a mechanistic model to describe sliding between two noncovalently bound filaments. For simplicity we rigidly fix one filament and consider only the motions of its partner. The moving filament is assumed to be a linear chain of identical units, each unit represented as a single particle. We assume particles move only along the filament axis, reducing the model to one dimension. Using Newton's classical equations of motion would neglect fluctuations in energy introduced by the surrounding environment. Instead, to simulate the canonical ensemble we use Langevin dynamics as a thermostat:

$$m_i \frac{dv_i(t)}{dt} = F_i(t) - \alpha v_i(t) + R(t) \tag{2.1}$$

$$\frac{dx_i(t)}{dt} = v_i(t) \tag{2.2}$$

The variable $x_i(t)$ represents position, $v_i(t)$ velocity, and m_i the mass of particle i. α is a friction constant with units of [mass/time]. The thermal force $R(t)$ is assigned a Gaussian distribution with a mean of $\langle R(t)\rangle = 0$ and covariance $\langle R(t)R(t')\rangle = 2\alpha k_B T\delta(t)$. When discretized into time steps of length Δt, the covariance becomes $\langle R(t)R(t')\rangle = 2\alpha k_B T/\Delta t$. $F_i(t)$ represents the force acting on the particle. This includes contributions from the rest of the filament, the neighboring filament, and an externally applied force. In our long one-dimensional chain, particles have an equilibrium spacing distance of l. We assume linear elasticity such that the energy of the bond of particle i with particles i-1 and i+1 is $U_{f,i} = \kappa_f((x_i-x_{i-1}-l)^2+(x_{i+1}-x_i-l)^2)/2$, where κ_f is filament stiffness. κ_f, is equal to AE_f/l, where A is cross-sectional area and E_f is the axial Young's modulus of the filament. The force exerted on displaced particle i is the negative of the spatial derivative of energy, $F_{f,i} = -\partial U_{f,i}/\partial x_i$.

Due to the repeating filament structure, energetic interactions of each particle with the rigid, bound filament are assumed periodic in x with a period of l. The peaks in this energy landscape might correspond to points of steric hindrance and high van der Waals energy, unfavorable electrostatic interactions or breakage of favorable electrostatic interactions, or reduced entropy due to motion constraints. Specifically, we define the energy $U_{b,i}$ of the ith particle as a sinusoid of period l. (See section 3.3 for a discussion of selecting the periodic function.) Twice its amplitude gives the transition energy U_a between minima, and a Taylor expansion about the minimum gives a local stiffness of $\kappa_b=2\pi^2U_a/l^2$. The resulting force on particle i is $F_{b,i} = -\partial U_{b,i}/\partial x_i$. Additionally, each particle is subjected to an externally applied force P_i, with energy $U_{P,i} = x_iP_i$. The force P_i may arise from the shear stress transmitted from surrounding filaments in a filament

bundle, and for uniform shear loading we assume constant $P_i = P$ uniformly for all particles. The total potential energy of particle i is $U_i = U_{f,i} + U_{b,i} + U_{P,i}$, and the force on particle i is $F_i = F_{f,i} + F_{b,i} + P$.

We nondimensionalize the equations of motion, taking as characteristic values mass m, length l, and the thermal energy setpoint k_BT_o. This gives rise to dimensionless variables $x^* = x/l$, $t^* = (k_BT_o/ml^2)^{1/2}t$, and $v^* = dx^*/dt^* = (m/k_BT_o)^{1/2}dx/dt$. From the governing equations, four dimensionless parameters arise:

$$P_P = \frac{Pl}{k_BT_o}; P_f = \frac{k_f l^2}{k_BT_o}; P_b = \frac{pU_a}{k_BT_o}; P_a = \frac{al}{\sqrt{k_BT_o m}} \tag{2.3}$$

Π_P, Π_f, Π_t, and Π_α may be considered dimensionless expressions of external force per particle, filament stiffness, transition state energy, and strength of coupling to the thermal bath (or viscosity), respectively. Defining a dimensionless thermal force R^* whose mean is zero and whose variance is $2\Pi_\alpha/\Delta t^*$ we can now rewrite the governing equations in dimensionless form.

$$\frac{dv^*_i(t)}{dt^*} = P_f\left(x^*_{i+1} + x^*_{i-1} - 2x^*_i\right) - P_b \sin\left(2\pi x^*_i\right) + P_P - P_\alpha v^*_i(t) + \left(\frac{2}{\Delta t^*}P_\alpha\right)^{1/2} N(t) \tag{2.4}$$

$$v^*_i = \frac{dx^*_i}{dt^*} \tag{2.5}$$

A script was written in C to numerically integrate Equations 2.4 and 2.5 using the leapfrog method. All parameters could be arbitrarily specified, including the number of particles and the time step. As an initial condition all particles were evenly spaced and positioned at a local energy minimum. Unless otherwise specified we use 16 particles and a time step of 10^{-4}. Select simulations repeated with a time step 10^{-5} yielded nearly identical results (not shown).

2.4.2 Time to failure

Nondimensional results were applied to RAD16-II using parameters consistent with the MD simulations: ß-strand spacing l = 4.8 Å, thermal energy $k_BT = 4.14 \times 10^{-21}$ J/K, and RAD16-II monomer mass m=1.713 kDa. In MD simulations, a friction constant of $\gamma = 5$ ps^{-1} (the *fbeta* parameter in CHARMM) was found to produce particle velocities whose autocorrelation had a decay time similar to that produced with the Nosé-Hoover thermostat in MD simulations (results not shown). Correspondingly, a viscous constant of $\alpha = \gamma/m = 1.42 \times 10^{-11}$ kg/ps was used in the coarse-grained model. Applied shear forces were exactly specified in the range of 576-720 pN per particle. Of the four dimensionless parameters, two are specified by the values above (Π_P = 61.3 to 83.4, and $\Pi_\alpha = 63$), leaving only Π_f and Π_b for tuning. These were varied and the quality of fit was manually checked to iteratively obtain a satisfactory fit.

Good agreement with MD results is obtained using $\Pi_f = 30$ and $\Pi_b = 95$ (Figure 2.7). Let us ask whether these values are physically reasonable. From the simulations described in Figure 2.3 we obtained a shear modulus of 1.8 GPa for strains < 4%, and from this we estimate the stiffness of the bond between ß-sheets. With shear occurring between ß-sheets whose backbones are about 10 Å apart, and a sheared area of 4.8Å x 60 Å per ß-strand, κ_b is 5.2 N/m, corresponding to a value of $\Pi_b = 46$, in order-of-magnitude agreement with our fitted value. Park et al. estimate that a two-ß-sheet filament exerts $1.6 \pm 0.6 \times 10^{-7}$ N per unit axial strain; for one ß-sheet over one period of 4.8 Å this corresponds to a stiffness of 167 N/m, or a nondimenesional stiffness of 9300. Π_f, the stiffness between alanine side chains on adjacent ß-strands, is much lower since the displacement can occur due to side chain flexing or rotation of the ß-strand in addition to

stretching of the backbone. Thus the values fitted values of Π_f and Π_b appear to be reasonable. All parameters defining the coarse-grained model are listed in Table 2.1.

In addition to accurately predicting mean time to failure, the behavior of coarse-grained model simulations was generally consistent with that of MD simulations of slippage. The center-of-mass trajectories exhibited discrete jumps in position analogous to the jumps in shear strain observed in MD simulations and shown in Figure 2.5.

Plotting the mean time to failure against the applied stress on a log-log scale shows a linear trend (Figure 2.8), regardless of chain length. This power law is consistent with the behavior of a single energetic trap observed by Evans et al. [75, 76]. For a given level of applied stress, time to failure also varies with the number of particles in the chain via a power law relationship. Intuitively, we understand that time to initiation of failure decreases as filament length increases, since the longer filament provides more sites at which initiation might occur. A best fit to a double-power law relationship gives the parameters in Equation 2.6 and the trend lines in Figure 2.8 (r^2=0.935).

$$t^* = \left(\frac{95.4}{\Pi_P}\right)^{17.4} \left(\frac{1}{n}\right)^{0.814} \tag{2.6}$$

The first factor in this equation has the form proposed by Evans et al., while the second factor is new and purely empirical.

With the fitted parameters, simulations are stable and consistent with a dimensionless time step as large as 0.01. With this time step, simulations run at about 300 dimensionless time units (or 4 ns) per hour, about 1500x faster than the corresponding MD simulations on a per-CPU basis.

We examined time-to-failure results' sensitivity to the model parameters. Results were most sensitive to changes in Π_b, with as much as an 8-fold increase in average

failure time resulting from a 10% increase in Π_b. This parameter determines the height of the energy barrier, so its importance is not unexpected. A 2-fold increase in filament stiffness Π_f increased average failure times as much as 5-fold, and a 2-fold increase in viscosity Π_α approximately doubled average failure times.

2.4.3 Contour of the energy landscape

While a sinusoidal energy landscape was used to produce the above results, the model behavior is similar with other suitable periodic functions. Five energy landscape functions were examined (Figure 2.9A). We designated these as the triangle wave (*V*), the sinusoid (*S*), the parabola with sharp cusps at the energy maxima (*U*), and parabolas whose cusps are smoothed with either 3rd- or 4th-order polynomials (*3o*) or (*4o*). *3o* is undesirable as it leaves an abrupt, flat curve over the cusp compared to the smoother *4o*. *V* is unique also in that its force is discontinuous at both the energy minima and the energy maxima. *U* and *4o* gave results very similar to the sinusoid *S* when the zero-force transition energy of the functions (as opposed to the stiffness about the energy minima) was matched (Figure 2.9B).

2.5 Discussion

Modeling has proven useful in understanding the mechanical behavior of protein filament bundles. For example, Bathe et al. have introduced a model to describe actin bundles formed from a host of actin-binding proteins (ABP's), based on the shear stiffness and spacing of these ABP's and the bundle diameter and length [77]. Buehler has investigated the properties of collagen fibers using a coarse-grained model that incorporates the failure strength of slippage between molecules, as obtained by MD [51]. We find that unlike Bathe's actin bundles, filaments of RAD16-II and other AFP's require consideration of interfilament slippage; and while Buehler's approach is

instructive, we find it useful to account for the significant time-scale dependence of failure strength when interpreting the results of MD simulations, which are generally restricted to ns or μs. Such short time scales are expected to exhibit unusually high failure strengths [78]. To our knowledge, the time dependence of failure strength has not been taken into account for protein filament bundles until the present study.

Many elements of our coarse-grained model appear in the literature. The Rouse model, for example, represents a polymeric filament as a chain of particles connected by springs and subjected to Langevin forces [79]. In a general sense, our model is also similar to all-atom (MD) or coarse-grained simulations using Langevin dynamics (e.g. [80]). All these approaches include discrete particles moving in a defined energy landscape according to Langevin dynamics. Our model differs from these, though, in its one-dimensionality. The model proposed by Bathe et al. [77] similar neglects deflection in directions normal to the filament axis but provides only a static solution of the shearing of filament bundles wherein no slippage occurs. Thus while our coarse-grained model relies on methods well established in the literature, it has combined these in a new way to model the deformation of sheared bundles of aligned filament that undergo slippage.

Park et al. [59] used thermal mode analysis and normal mode analysis to determine that the tensile stiffness of RAD16-II at $1.6\pm0.6 \times 10^{-7}$ N (where stiffness is unusually defined as resisting force per unit strain.) For one filament's cross-sectional area of about 17.5 Å x 60 Å, this gives a Young's modulus of 9.5-21 GPa. In an isotropic, incompressible material the shear modulus would be one third of this value, 3.2-7.0 GPa. We found the shear modulus between tightly stacked filaments to be only 1.8 GPa, and the inclusion of water-filled voids might lower the modulus and increase the anisotropy

even further. Given the inherently anisotropic structure of filament bundles, this is not a surprising result. Anisotropy has been documented for other bundled filaments such as microtubules [81] and single-walled carbon nanotube ropes [82].

While MD simulation is suitable for obtaining the elastic properties of a system the size of ours (7500 to 15,000 atoms), obtaining failure data is a greater challenge. Failure time is a stochastic function of the applied load; or conversely, failure strength is a function of observation time. For results of MD simulations--generally nanoseconds in duration--to be applied to ordinary time scales, this time dependence must be accounted for. We have done so in two ways. First, using a coarse-grained model allows us to run more simulations and to extend them to longer times than would be feasible using MD. Second, we have fit the simulation results with Equation 2.6 to predict behavior at time scales unattainable even with coarse-graining.

At each of these steps, efficiency is obtained at the expense of detailed information. MD simulations comprising 7500 atoms, each with independent 3-dimensional motion, are mimicked by a coarse-grained model of 16 particles moving in one dimension. Fitting an equation to the failure times obtained from simulations reduces the system further such that no information on individual particle motion remains. This approach assumes that the failure mechanism on a time scale of seconds is the same mechanism as occurs in nanoseconds, a postulation that can only be verified when model predictions are confirmed by experiment. Such coarse models are necessary to bridge the gap between the atomistic detail obtainable only in MD simulations and the much larger time and length scales accessible by experimental techniques.

A previous analysis by Leon et al. [42] modeled the AFP gel EFK8 as a cellular solid composed of isotropic elastic beams which deform primarily in bending. This analysis found the bulk properties of EFK8 consistent with a filament Young's modulus of ~1 MPa, whereas Park et al. [59] found the axial Young's modulus of RAD16-II filaments to be about 1000× this value. The results from the present study allow us to explore and shed some light on this discrepancy. Three potential explanations are as follows:

(1) Anisotropy makes the filament bundles more compliant in shear such that bending is no longer the dominant mode of deformation.

(2) Adhesion between filaments is sufficiently weak that slippage occurs in the filament bundle to relieve stress even for small strains at the bulk level.

(3) Imperfections or void spaces within the filament bundles are sufficiently common that filament bundles cannot be modeled as a monolithic beam.

The following analysis suggests that explanations (1) and (2) are unlikely, while explanation (3) is plausible. The prevalence of void spaces or packing imperfections will remain a subject for future studies.

The modeling approach of Gibson and Ashby [10] for mechanical analysis of cellular solids has been successfully applied to a wide range of porous materials, including protein filament networks [42, 83]. Given the Young's modulus of the material's solid fraction, this modeling approach enables a rough estimate of bulk Young's modulus by analyzing a unit cell with typical microstructural dimensions. Employing the cellular solids model, we consider a unit cell wherein a filament bundle of RAD16-II is loaded by intersecting fibers as in Figure 2.10A. Figure 2.10B shows the

idealized loading condition, where moments and shear are resisted at both end points and a load P is applied at the filament bundle's center. At the inflection point halfway between the end and the center, the moment falls to zero. This enables us to model each segment of the filament bundle as a cantilevered beam with a lateral applied load of $P/2$ at the tip (Figure 2.10C). Elementary beam theory predicts that

$$\frac{\delta}{2} = \frac{(P/2)(L/4)^3}{IE_f} \tag{2.7}$$

where $\delta/2$ is the deflection of the tip of the beam due to bending, $(P/2)$ is the applied force, $L/4$ the length of the cantilevered beam, and I the moment of inertia. For a circular cross section, $I = \pi d^4/64$, where d is the beam diameter. In an RAD16-II gel, where a typical pore size is L=~300 nm and typical filament bundle diameter d=~30 nm [40], we predict a tip deflection $\delta/2 = 0.18P$, or a deflection of $\delta = 0.35P$ at the midpoint, for P in nN and δ in nm. Referring again to the cellular solids model, we note that bulk strain scales as $\varepsilon \sim \delta/L$ and bulk stress as $\sigma \sim P/L^2$, giving a bulk Young's modulus of $E_b = \sigma/\varepsilon = P(L/4)^3/IE_f$. (The subscripts f and b are used to distinguish between filament and bulk properties.) By algebraic manipulation we find

$$E_b = k\left(d/L\right)^4 E_f \tag{2.8}$$

where k is a constant of order 1. This predicts for RAD16-II a Young's modulus of E_b ~ 1 MPa, an over-estimation based on the experiments by a factor of 100-1000.

Could this discrepancy be due to the mild anisotropy of cohered RAD16-II filaments found in the present study (explanation 1)? Consider that our cantilevered beam may deflect not only in bending but in shear, and that a low shear modulus makes this deflection greater than it would be in an isotropic material. However, deflection due

to shear, $\delta_{shear}=(P/2)(L/2)/AG$ (A is the cross-sectional area, G is the shear modulus of 1.8 GPa), is small, less than 10% of bending deflection even after accounting for anisotropy. The anisotropy of tightly packed filament bundles therefore fails to account for the compliance of RAD16-II gels.

Is the shear load resulting from small bulk strains sufficient to cause slippage between filaments of RAD16-II (explanation 2)? While points of slippage failure may propagate within a filament bundle, the grain boundaries found at junctions between filament bundles would stop the failure propagation. Since the spacing between these junctions is about 300 nm and the diameter of the filaments 30 nm, we take the maximum failure surface to be the area 300 nm x 30 nm = 9000 nm^2. Each particle in our coarse-grained model represents an area of 0.48 nm x 6 nm = 2.88 nm^2. We can conservatively assume that the number of particles on a failure surface will not exceed 9000/2.88 = 3125. We apply Equation 2.6 to ask what level of shear stress could cause failure on a surface of this size on ordinary time scales of $t \sim 1$ s ($t^* = 8x10^{10}$) and find that a shear load of 45 MPa (Π_P=15) is needed.

Using the cellular solids model outlined above, we estimate that a load of $P = 10$ nN (or $\sigma = 444$ kPa) produces a 10% bulk strain. Under the loading conditions of Figure 2.10, the average shear across the filament bundle is $\tau_{ave}= P/2A = 7$ MPa. The maximum shear in a beam with a circular cross section is $\tau_{max} =1.5\tau_{ave}= 11$ MPa. Even under conservative assumptions, then, the shear load is not sufficient to produce slippage in a tightly packed filament bundle.

Consider now explanation (3), that filament bundles are either not monolithic or have weak points due to packing imperfections. We repeat the cellular solids analysis

treating each filament bundle not as a single beam but as many independent smaller beams. Each filament has a cross-sectional area of about 12 nm^2, corresponding to an effective diameter of about d=4 nm. In a 30-nm bundle, with cross-sectional area 700 nm^2, about n=50 individual filaments exist. Equation 2.8 becomes

$$E_b = kn(d/L)^4 E_f \tag{2.9}$$

where k is a constant of order 1. Taking E_f to be 15 GPa this gives a bulk Young's modulus of ~24 kPa, on the order of experimental results, e.g. by Leon et al. [42]. Thus, experimental and theoretical results are consistent if bundled filaments do not transfer significant shear between one another and bend independently rather than as a monolithic beam. This would be expected if the internal structure were random rather than the highly ordered arrangement assumed in the previous analysis. In this scenario, the charged groups interact only loosely, and are therefore free to slide relative to one another. Further investigations of the fiber internal structure will be needed to confirm this hypothesis.

These predictions suggest two potential means for increasing the modulus of AFP gels. One is to enhance the extent to which the filaments align in the idealized fashion with the hydrophilic side groups optimally matched. In this instance, the gel bulk modulus could increase, approaching the 1 MPa prediction from Equation 2.8. While this might seem challenging, there is evidence with a different peptide sequence that fibers can be formed that exhibit ordered structure on a scale of microns, although the geometry of these fibers is more sheet-like than cylindrical [84]. A second, perhaps more feasible approach would be to introduce a cross-linking agent that bridges between filaments internal to the fiber, producing a gel modulus somewhere between the two limiting cases

presented above. For this strategy, the cross-linking agent should be much smaller than the previously used streptavidin [68] or transglutaminase [44], to ensure that it accesses the core of the fiber.

2.6 Conclusion

We have demonstrated that noncovalently bundled filaments may exhibit elastic behavior at low stresses and small displacements, with mild anisotropy. Higher loads may introduce inelastic deformations associated with transitions between minima of free energy. The frequency of inelastic slippage between closely cohered filaments is a stochastic function of shear stress and the size of the loaded surface. Extrapolating simulation results to the time scale of seconds with conservative assumptions, we found that filament bundles are not likely to commonly fail under less than 45 MPa of shear. An approximate analysis based on a cellular solids model shows, however, that tightly adhered filament bundles would experience a maximum shear stress of only about 11 MPa, while the shear stress in bundles with void spaces would be lower still. We conclude that neither filament anisotropy nor slippage between adhered filaments can satisfactorily account for the low bulk Young's modulus of RAD16-II or other AFP gels. However, if bundled filaments are assumed to be well lubricated (e.g. by included water), the bulk Young's modulus and the Young's modulus of RAD16-II filaments are consistent.

Table 2.1
Parameters of the coarse-grained model of interfilament shear

Parameter	**Fitted value**	**Description**
Π_P	61.3-83.4	Applied shear
Π_f	30	Tensile stiffness
Π_b	95	Shear stiffness between bound ß-sheets
Π_α	63	Strength of coupling to thermal bath

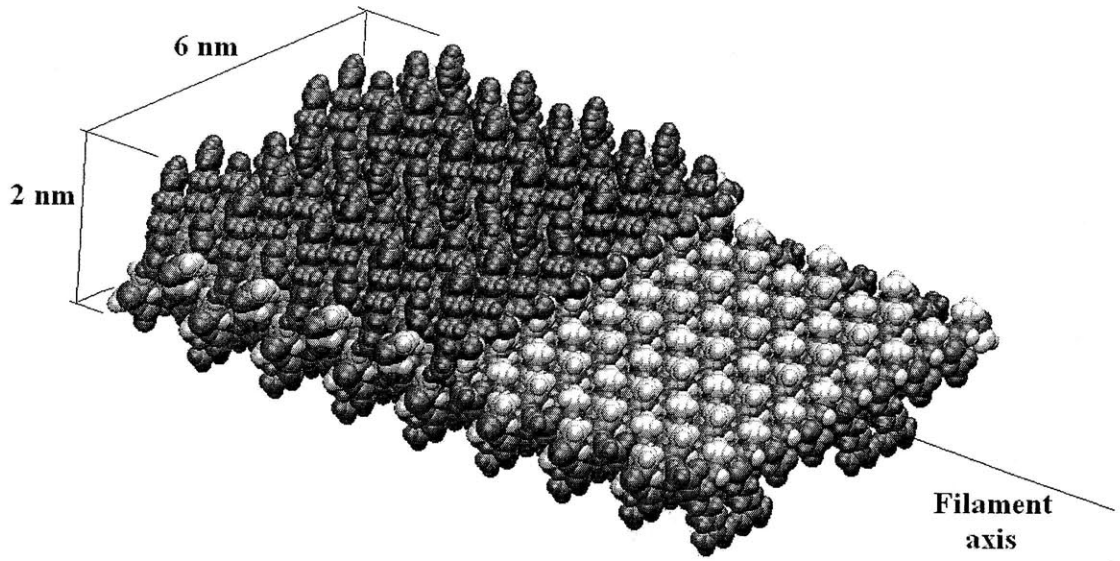

Figure 2.1. A filament of RAD16-II comprises two β-sheets, each with a hydrophobic surface of alanine side chains oriented toward the filament center, and an outer hydrophilic surface of arginine and aspartic acid side chains. A filament has a roughly rectangular cross-section. Here the upper β-sheet is cut away to show the hydrophobic core.

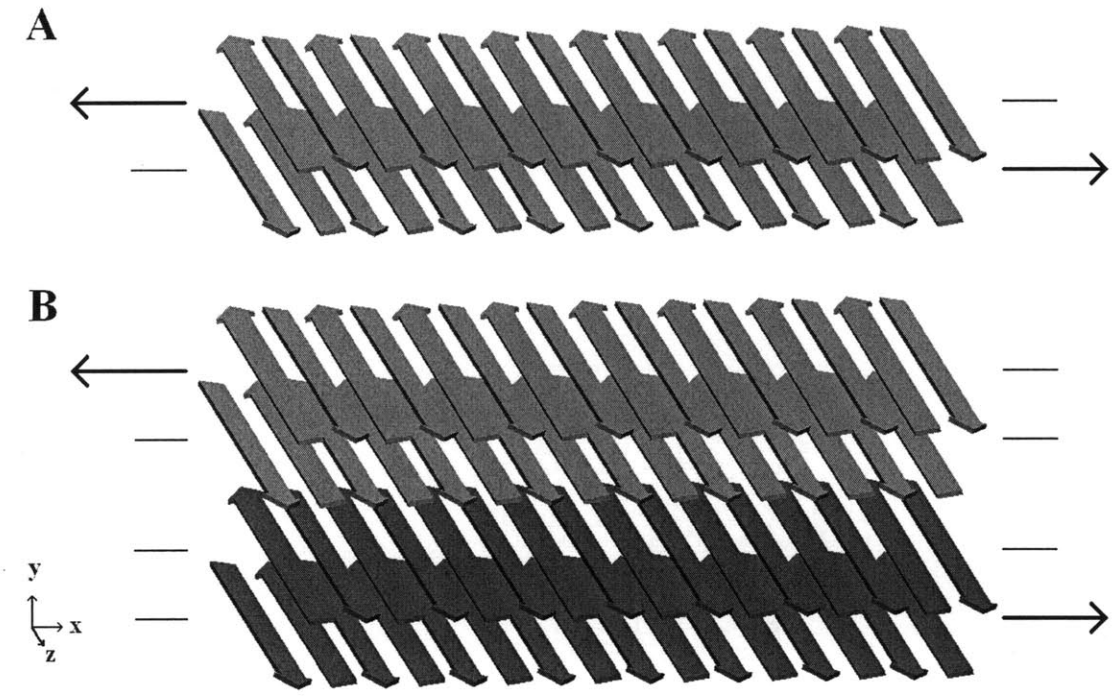

Figure 2.2. Shear loading schemes for one (A) or two (B) double-layered filaments are shown. (A) Shear stress is applied over the hydrophobic surface at the core of a single filament. (B) Shear stress is applied over the hydrophobic core of each filament and the charged surface between the filaments. In each case a constant force is applied to the α-carbons in one β-sheet, and an opposite force to the α-carbons of another β-sheet. Forces are directed along the filament axis.

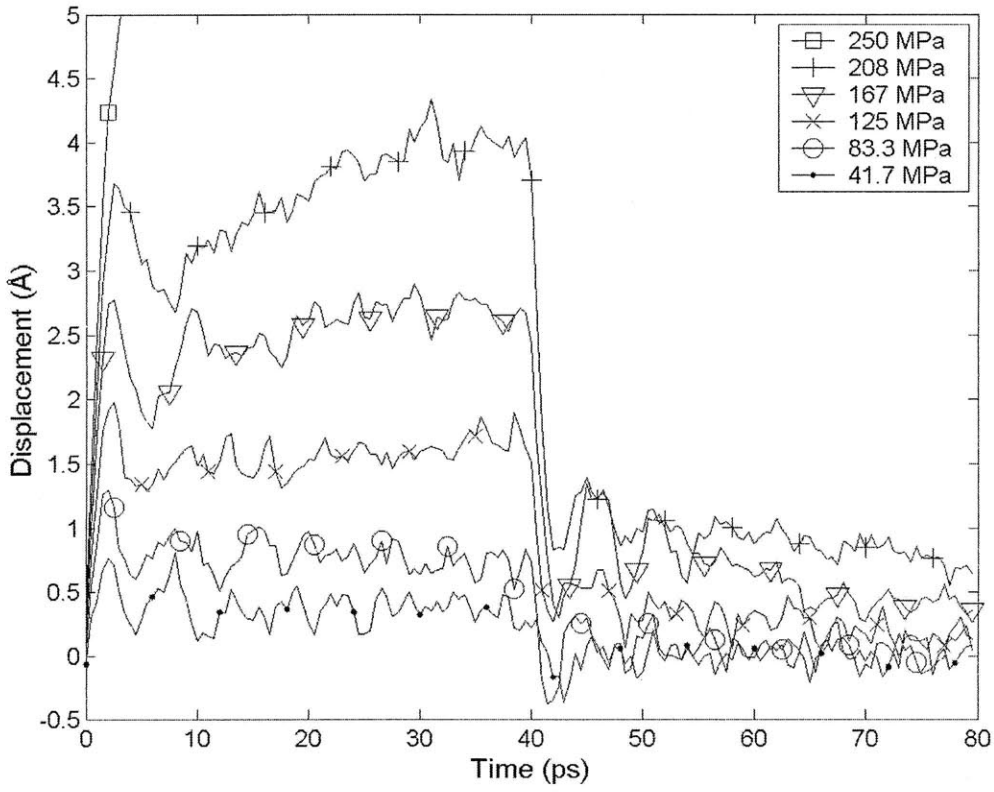

Figure 2.3. Under small shear loads the shear deformation of RAD16-II filaments (loaded as in Figure 2.2B) is elastic. Under 250 MPa of applied shear, the filaments slip irreversibly within a few ps.

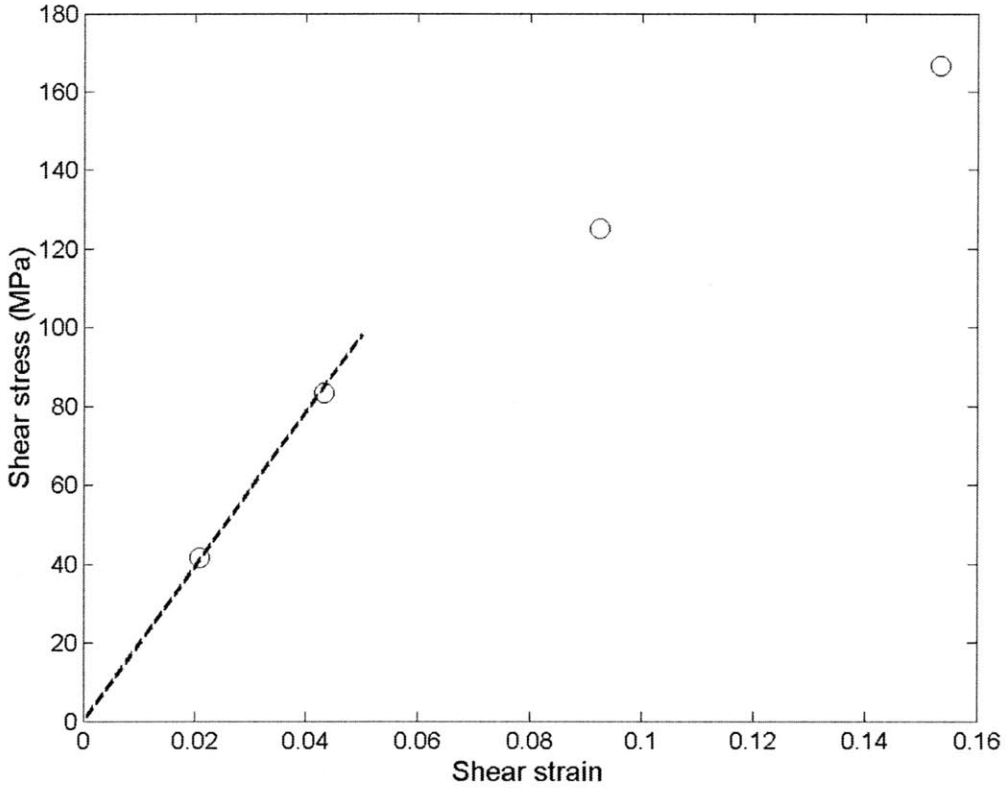

Figure 2.4. The trajectories in Figure 2.3 exhibit a linear stress-strain relationship only up to about 5% strain. In this low-strain region, the shear modulus is 1.8 GPa. At larger strains, strain softening occurs.

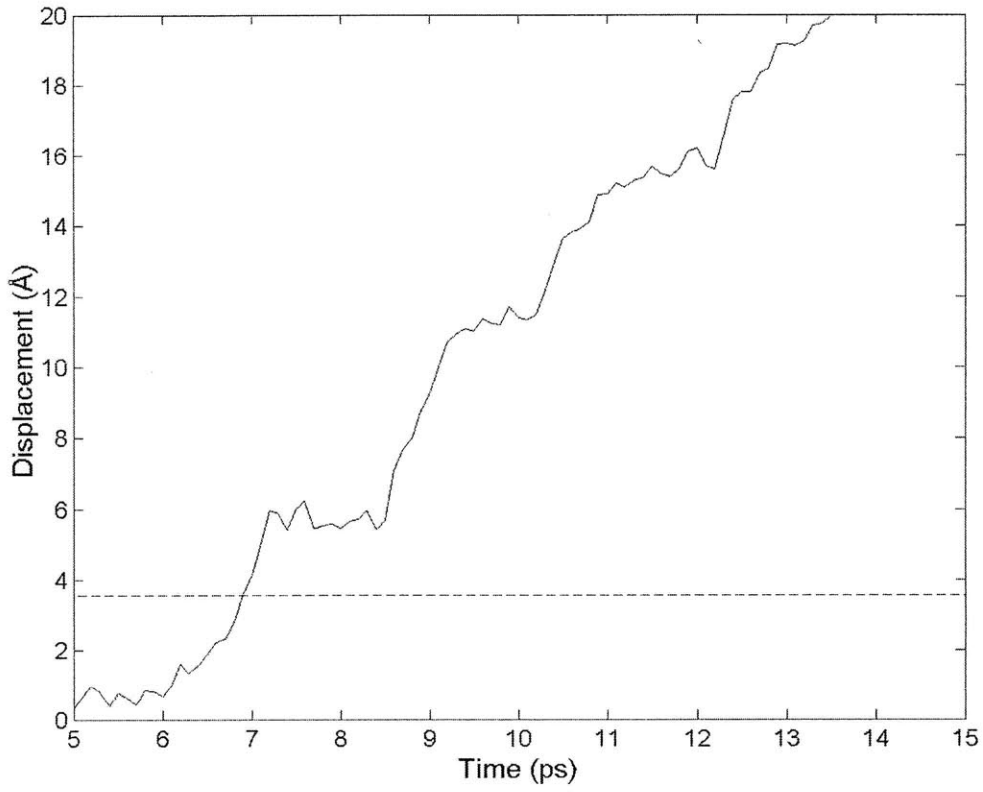

Figure 2.5. The trajectory of the methyl carbon in an alanine side chain is shown as the hydrophobic core of an RAD16-II filament is forced to slip. The discrete jumps indicate energy minima with a spacing that corresponds to the 4.8 Å between ß-strands.

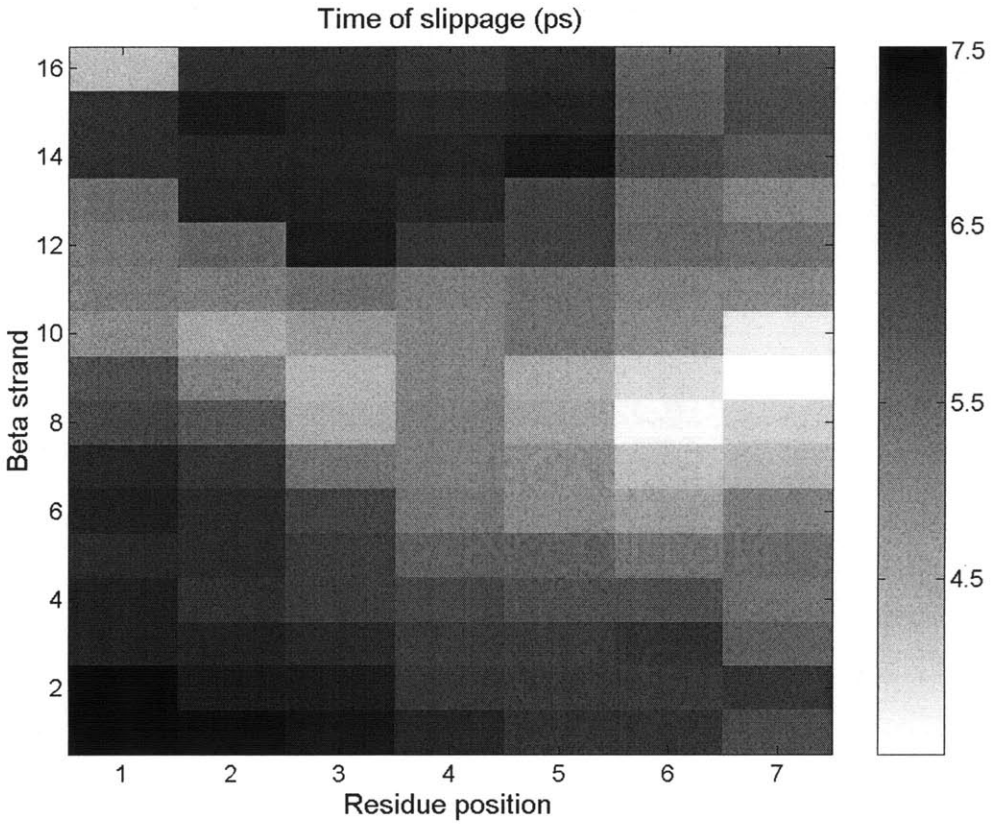

Figure 2.6. The hydrophobic surface of a filament of RAD16-II is represented, with each pixel representing one alanine side chain. Failure initiates at the white-colored points, then propagates laterally and longitudinally to the rest of the surface.

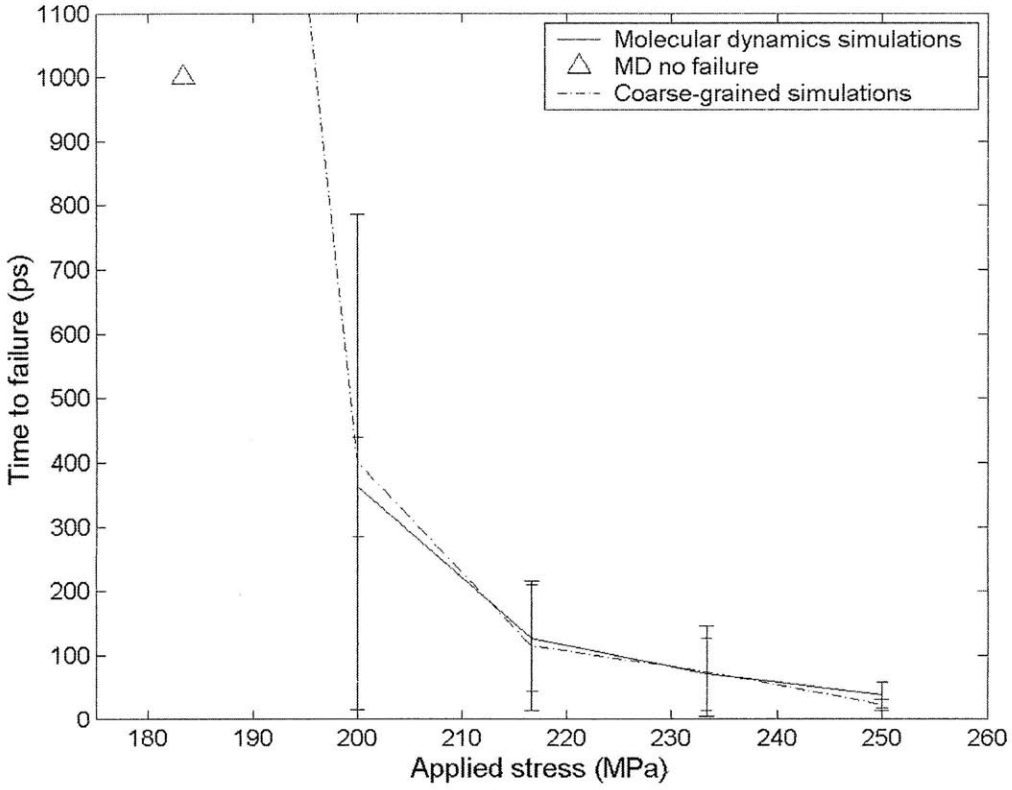

Figure 2.7. The time from when a load is first applied to when failure occurs is plotted against the applied shear stress for both MD simulations (n=3) and coarse-grained simulations (n=100). The triangle indicates MD simulations terminated before failure occurred (n=3). At 183 MPa the coarse-grained simulations had a mean failure time of 2935 ps, standard deviation 2552 ps.

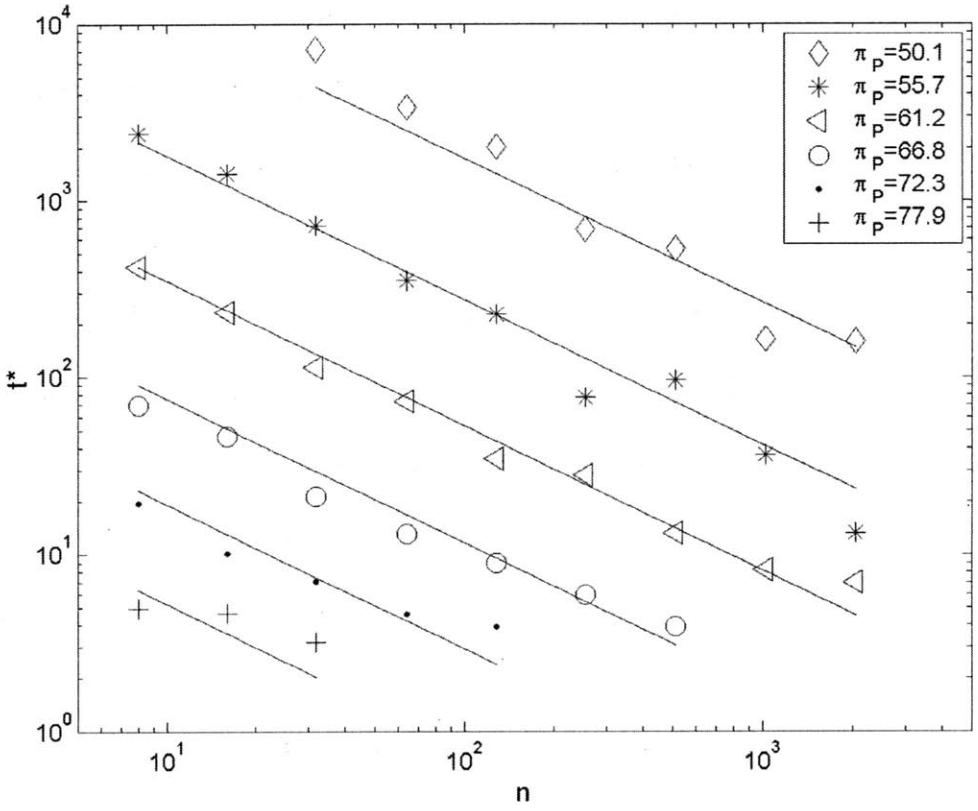

Figure 2.8. In coarse-grained simulations, a power law was found to relate time to initial failure to applied load and to the number of particles simulated. The lines show a global best-fit described by Equation 2.6, with r^2=0.935.

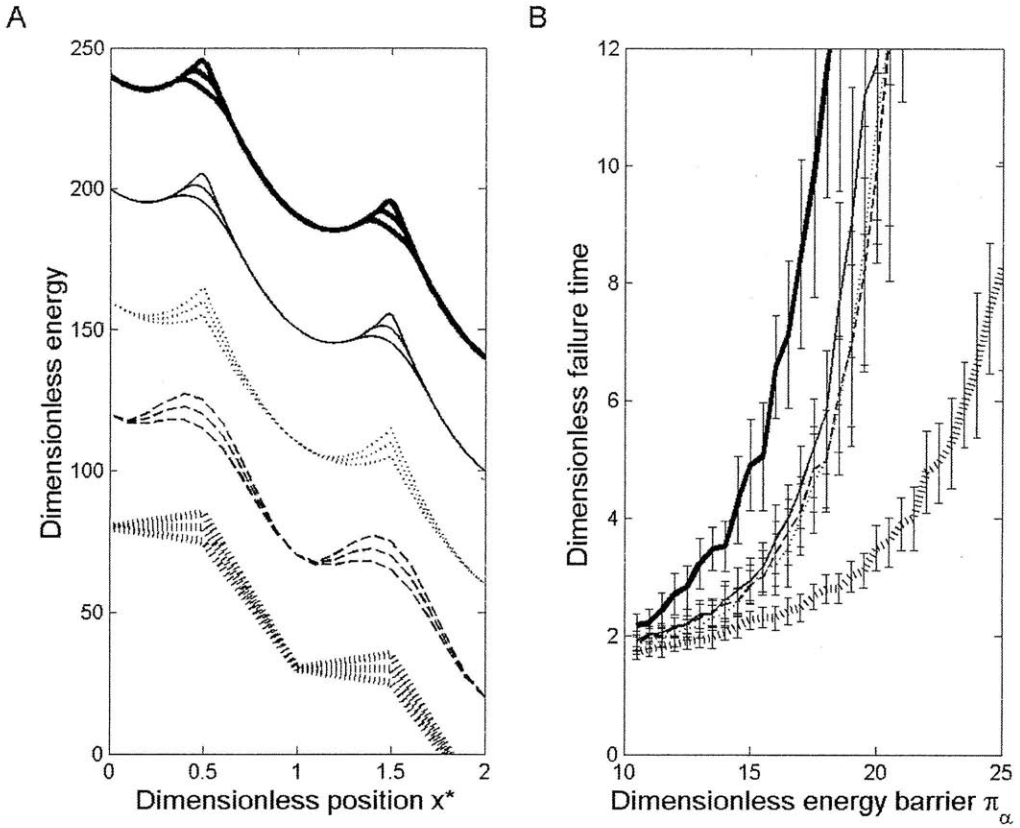

Figure 2.9. (A) Five periodic energy functions are shown, with arbitrary positioning on the y-axis. Each is shown with dimensionless energy barrier Π_b set to 30, 25, and 20 for illustration, all under a dimensionless load of $\Pi_P = 50$. From top to bottom these are 3o, 4o, U, S, and V, as defined in the text. (B) Dimensionless time to failure is plotted from simulations performed with a system of 16 particles using each energy function over a range of values for Π_b. Each line style matches that of the function in (A) used to generate it.

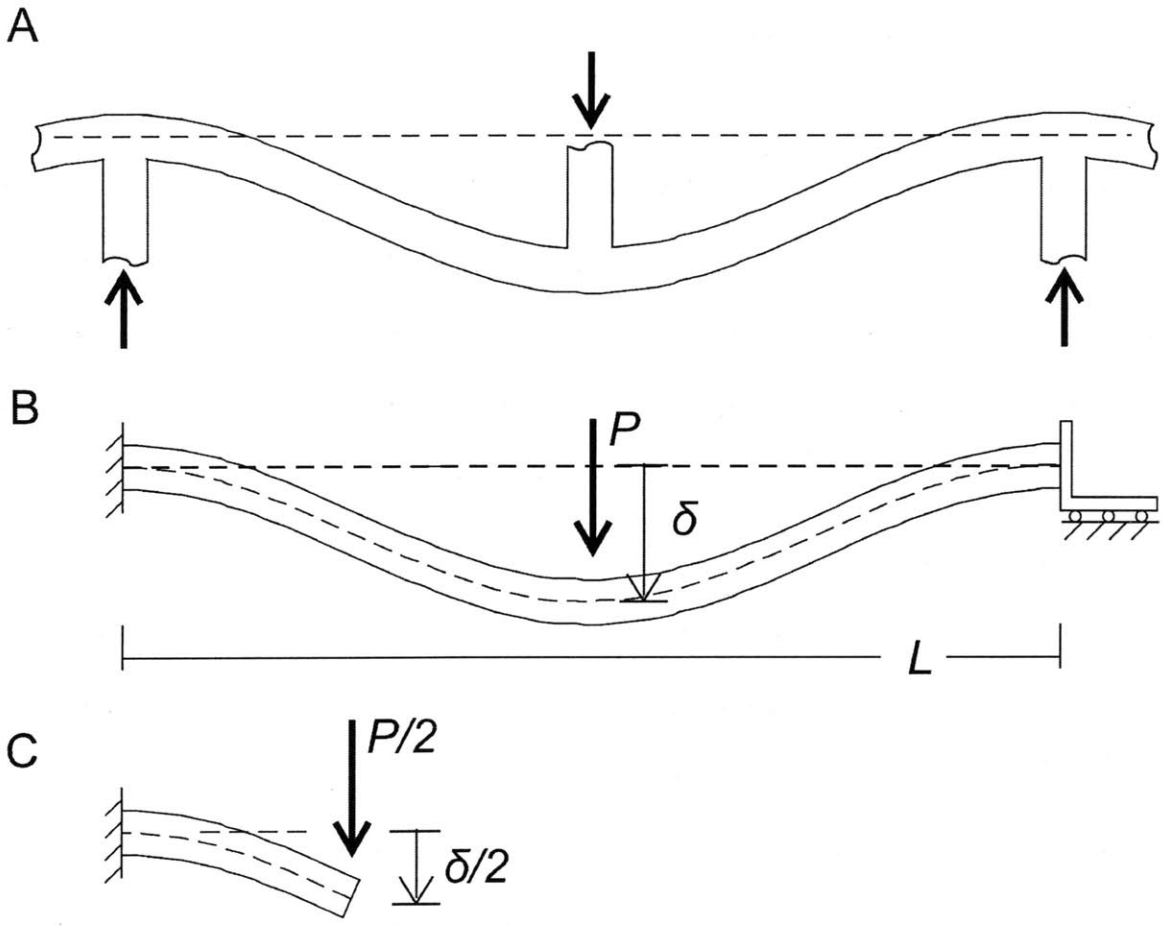

Figure 2.10. (A) When a load is applied to an RAD16-II gel at the bulk level, the load is thought to be borne at the microstructural level by the bending of filament bundles as they are loaded at their points of intersection. (B) This bending is idealized as a beam whose ends are fastened such that they resist both moments and shear, and whose center is loaded by force *P*. (C) The problem may be simplified by noting that each quarter of the beam is loaded as a cantilevered beam with a shear load but no moment at the tip.

Chapter 3 Mechanical characterization of self-assembling peptide hydrogels by microindentation*

Hydrogels formed from self-assembling synthetic oligopeptides have been studied for almost 2 decades for use in tissue engineering and drug delivery. While a great deal has been learned about the microstructure of these materials, there remain questions about how peptide filaments are ordered to form a gel. These unanswered questions leave a disconnect between our understanding of the observed nanoscale mechanical properties of peptide filaments and the macroscale properties of the gels they constitute. This study attempts to bridge this gap by examining the role of filament length and interfilament cross-links in determining bulk mechanical properties measured my microindentation, and provides the first thin-section transmission electron microscopy images of self-assembling oligopeptide gels embedded in resin. The results suggest a gel structure in which filaments are not densely bundled as previously believed. They also demonstrate for the first time that cross-linking can be an effective strategy to increase the stiffness of self-assembling oligopeptide gels.

3.1 Introduction

Hydrogels have long been recognized for their use as drug delivery vehicles [3], cellular scaffolds for tissue engineering [85, 86], and "smart" materials that respond to environmental cues [4]. Since many of these applications require materials that are porous and thin enough for efficient diffusion and cell penetration, hydrogels tend to have relatively poor mechanical characteristics, which may limit their usefulness in many applications. Therefore, in developing new hydrogel materials, characterization and control of mechanical properties should play a prominent role.

---

* Material from this chapter has been submitted for publication in a peer-reviewed journal. Nathan A. Hammond and Roger D. Kamm, 2010.

Common methods for measuring a gel's mechanical properties include rheometry, tensile testing, and microindentation. Tensile testing of weak hydrogels is technically challenging and typically requires specialized equipment built in-house [41, 42, 87], making it difficult to reproduce the results of other researchers. Rheometry is a widely used method for mechanical characterization of gels under dynamic loading in shear. However, it is not well suited for obtaining compression or failure data. The sample volume for these techniques is relatively large (e.g. 70 μl for rheometry [40], 1 ml for tensile testing [41]), which is an important consideration for precious materials. Both methods require materials to be in a precise format, making them of limited use for tissue samples or for materials not formed in the format required for measurement.

Over the last decade, nano- and microindentation have become widely used for the characterization of gels [46], thin films [47], tissue specimens [48], and even individual cells [49]. Dimitriadis et al. have shown good correlation between indentation and rheometry, especially when using colloidal probes with a precisely known, large radius (5 μm) [47]. Indentation methods may be used to observe effects not measurable by standard rheometry, including poroelasticity [13], and plastic failure [50].

In the present study we examine the self-assembling peptides RAD16-I (PuraMatrix^{TM}) and KLD-12. Both RAD16-I (sequence Ac-$[RADA]_4$-$CONH_2$) and KLD-12 (Ac-KLDLKLDLKLDL-$CONH_2$) have an alternating pattern of hydrophobic (alanine or lysine) and hydrophilic (arginine or lysine, and aspartic acid), amino acids. The hydrophilic groups have a pattern of charge that is self-complementary when peptides are aligned in an antiparallel β-sheet, such that oppositely charges side chains are juxtaposed. This results in extremely stable β-sheet filaments [35] that aggregate

under pH-neutral conditions to form macroscopic gels [37]. These and other oligopeptides exhibiting similar structure and behavior are reviewed by Zhang [24]. RAD16-I has been studied for many applications as a cell scaffold, including variations with attached binding motifs or biotin-streptavidin links to bioactive molecules [28, 88], or with an MMP-cleavable sequence to promote cell migration [89]. KLD-12 has been used as a scaffold for cartilage tissue engineering [26, 90, 91].

Our interest in the mechanical properties of self-assembling oligopeptide gels is two-fold. First, we aim to develop practical strategies to vary the stiffness of gels so that cell scaffolds can be prepared with mechanical properties that vary over a useful range. Second, we aim to elucidate the fundamental mechanisms governing the mechanical properties of these gels, which remain poorly understood. For example: 1) it is still unknown whether protein filaments form a loose mesh or adhere together in dense bundles; 2) the role of filament length in gel mechanical properties remains undetermined; 3) efforts to stiffen gels by cross-linking have surprisingly not been found effective [44, 68], but the reason for their failure is not understood.

To achieve these aims we use microindentation for mechanical characterization of gels, atomic force microscopy (AFM) for observation of individual peptide filaments, and thin-section transmission electron microscopy (TEM) of gels embedded in resin to characterize the gels' microstructure.

3.2 Methods

3.2.1 Materials

RAD16-I and KLD-12 were synthesized courtesy of 3DM, Inc. (Cambridge, MA). Peptide stock solutions were provided at a 10 mg/ml concentration. Peptide solution was stored at 4°C until use.

3.2.2 AFM imaging of filaments

Peptide solution was sonicated (Sonics Vibra-Cell, Newtown, CT) at 50% power for 90 s. Samples were taken immediately after halting sonication ($t = 0$), or at varied times up to t=24 hours later. Peptide solution was diluted to 0.01 mg/ml in 0.01 M HCl. The dilute peptide solution was shaken vigorously for 20 seconds before 5 µl peptide was pipetted onto a freshly cleaved mica surface. After 20 s incubation, the mica was rinsed with 500 µl of deionized water and wicked dry with a tissue. Samples were then left to fully dry and were scanned within 24 hours on an Asylum (Santa Barbara, CA) MFP-3D atomic force microscope in AC (tapping) mode using a µMasch model NSC16 probe (San Jose, CA), with a nominal 170 kHz resonant frequency and 10 nm tip radius.

3.2.3 Preparation of polyacrylamide gels

A 5% solution of 37.5:1 acrylamide:bis-acrylamide (Bio-Rad, Herculus, CA) in water was degassed in a vacuum chamber for 30 min. 60 µl of 10 mg/ml ammonium persulfate (Bio-Rad) in water and 20 µl TEMED (Bio-Rad) were added to 1 µl of polymer solution and mixed by vigorously shaking. 310 µl of this solution was pipetted onto a rheometer plate at room temperature to gel as a disk 20 mm in diameter and 1 mm thick under the lowered rheometer head.

3.2.4 Rheometry

Gelling of the polyacrylamide was monitored by applying a 1-Hz sinusoidal load on an AR 2000 rheometer (TA Instruments, New Castle, DE) with a 20-mm parallel plate geometry at 5% peak strain every minute for 30 minutes, sufficient time for the storage modulus G' to plateau. A frequency sweep was then performed from 0.1 to 10 Hz at 5% strain.

3.2.5 Preparation of peptide gels for microindentation

Washer-shaped molds were made from a 1.1-mm sheet of polycarbonate plastic using circular punches (inner diameter 3.2 mm, outer 11 mm). To contain peptide while allowing diffusion of phosphate buffered saline (PBS) from outside, a piece of backing paper (nitrocellulose membrane, Pall LifeSciences, Port Washington, NY) was affixed to one side of each mold with high-vacuum grease (Dow Corning, Midland, MI). The mold was placed in a 35-mm culture dish (BD Biosciences, San Jose, CA) with the paper downward on a piece of Kimwipe tissue (Kimberly Clark, Irving, TX) soaked with Dulbecco's PBS (Lonza Biowhittaker, Walkersville, MD). The mold was then filled with 12 μl of peptide solution freshly sonicated (Sonics Vibra-Cell, Newtown, CT) at 50% power for 90 s, and the culture dish was closed and sealed with Parafilm M (Pechiney Plastics Packaging, Menasha, WI). One hour later the dish was opened, the gel was covered with PBS, and the dish was again sealed. Indentation measurements were taken after 24 hours incubation at room temperature.

3.2.6 Microindentation of gels

AFM tips for microindentation were prepared by gluing one 10-μm diameter polystyrene bead (Polysciences, Warrington, PA) near the tip of each AFM cantilever (model TR400PSA, 80 pN/nm, Asylum Research, Santa Barbara, CA) with Loctite 3211 light cure adhesive (Henkel, Dusseldorf, Germany) and placing under an ultraviolet lamp (Raytech Industries, Middletown, CT) for 1 hour. Tips were calibrated in PBS on an Asylum MFP-3D atomic force microscope (Santa Barbara, CA) using the thermal calibration method [92]. Measurements were collected from triplicate samples of each gel type. A force-indentation curve was collected from 20 random points on each gel by

bringing the tip in contact with the gel at a rate of 5 μm/s up to a trigger force of 10 nN before retracting.

The relationship between force and indentation depth for a rigid sphere (approximated as a parabolloid) impacting an ideal elastic solid is given according to Hertz contact theory in Equation 3.1 [93], where F is force, G is shear modulus, υ is the Poisson ratio, R is the radius of the sphere, and δ is the indentation depth into the material. To obtain the shear modulus from the force-indentation data, an in-house MATLAB (Natick, MA) script was used to find a least-squares fit of Equation 3.1 to the approach curve by varying the force and displacement offsets (values of F and δ taken as 0) and the shear modulus G. The bead radius is 5 μm. Poisson's ratio υ is taken as 0.5. (Experimental measurements of Poisson's ratio in hydrogels typically fall in the range 0.4-0.5, e.g. [94, 95]).

$$F = \frac{8G}{3(1-\nu)} R^{\frac{1}{2}} \delta^{\frac{3}{2}} \tag{3.1}$$

3.2.7 Thin-section TEM of peptide gels

KLD12 and RAD16-I gels were prepared as for microindentation.experiments in PBS from peptide solutions 24 h after sonication. Gels were stained with 2% osmium tetroxide (Electron Microscopy Sciences, Hatfield, PA) in 1.5% potassium ferrocyanide (Fisher Scientific, Fair Lawn, NJ) for 2 h, dehydrated in a graded series of solutions up to 100% ethanol, and embedded in Epon-Araldite (Electron Microscopy Sciences, Hatfield, PA). 90-nm thin sections were cut and stained with uranyl acetate (Fisher Scientific, Fair Lawn, NJ), and examined using a transmission electron microscope (Model 300, Phillips, Eindhoven, The Netherlands) at 20,000× magnification.

3.2.8 Statistical analysis

3 distinct samples were prepared and measured for each type of gel, and 20 measurements were collected from different points on each. All the estimates of shear modulus from a single gel sample were averaged and treated as one data point. Student's t-test was used for comparison of means and testing significance of the slope in a linear fit. For multiple pairwise comparisons, one-way ANOVA was performed, and the Tukey method for multiple comparisons was carried out using MATLAB.

3.3 Results

3.3.1 Filaments disrupted by sonication regrow linearly with time

Peptide solutions were sonicated and then incubated at room temperature for varying lengths of time (0-24 h) before depositing filaments on a mica surface for observation by tapping mode AFM. The lengths of filaments in each AFM scan were quantified using a MATLAB script written in-house, which allowed a user to manually trace each filament in an image. The code was validated using computer-generated images similar in appearance to the AFM scans, and measured lengths agreed well with the length distribution specified when generating the images (results not shown).

Immediately after sonication, RAD16-I filaments are relatively short, and their average length increases gradually with time (representative images in Figure 3.1). Over 24 hours the filament population shifts from a large number of short (120 nm average) filaments to a smaller number of filaments with a significantly greater average length (540 nm) (Figure 3.2). The increase in mean filament length is approximately linear in time (r^2=.97), with mean peptide length increasing at about 17 nm/h.

3.3.2 Thin-section TEM reveals void spaces between filaments

TEM images of 90-nm sections of RAD16-I and KLD-12 gels are shown in Figure 3.3. In both gels, filamentous structures about 10 nm wide and globular structures up to 200 nm in diameter are visible, consistent with filaments and globules observed by AFM (Figure 3.1). The distribution of stained matter is inhomogeneous, with some regions populated with clustered filaments and other regions mostly void. The pore size between dense regions is roughly 300 nm. Even in the densest regions, individual filaments are not closely packed, and most of the volume is void space between filaments. Filaments appear somewhat aligned in one dominant direction, but many non-aligned filaments are present.

3.3.3 Validation of microindentation method

We indented gels using a 10-μm-diameter bead attached to an AFM cantilever. The force-displacement profile during indentation was used to characterize the mechanical properties of the gels. Since local mechanical properties can vary widely in peptide gels we tested this method first using a polyacrylamide standard with a storage modulus of comparable magnitude to our peptide gels, and with little frequency dependence from 0.1-10 Hz (not shown). Seven AFM tips were prepared with beads and each calibrated separately, and force-indentation curves for a polyacrylamide gel were collected with each tip. The gel exhibited elastic behavior with little hysteresis (Figure 3.4), and the results were well described by Hertz theory of Equation 3.1 (r^2>.99). The mean of all shear modulus measurements is 434 Pa. This is in good agreement (16% difference) with a storage modulus of 517 Pa measured in the same gel by parallel plate rheometry (1 Hz, 5% strain). Standard deviation between the means obtained from measurements by each of the 7 tips is 40 Pa, indicating ~10% variation attributable to tip

preparation or calibration procedures. Standard deviation of the measurements taken with a single tip is on average 21 Pa or ~5%, giving a measure of the variation between individual measurements with the same tip or the variation between locations on the polyacrylamide gel. The fact that this variation is much smaller on polyacrylamide than on peptide gels (Figs. 6, 7) indicates that the variation between peptide gel measurements is caused principally by inhomogeneities in the gels (either bulk or surface) rather than variability inherent in the measurement technique.

3.3.4 Characterization of RAD16-I gels with varied concentration

Typical force-displacement curves for RAD16-I gels are presented in Figure 3.5. The presence of hysteresis in these curves indicates energy absorption over a loading-unloading cycle. Adhesion between the probe and the gel is evidenced by a region of negative force in the unloading curves, and this adhesion is at least partially responsible for the hysteresis. As an approximation, we estimated the shear modulus from the loading portion of the force-displacement curves and used this as a metric for comparing the stiffness of different gels. Increasing the peptide content of RAD16-I gels from 3 to 10 mg/ml increased the mean shear modulus by almost 7-fold, as shown in Figure 3.6. The mean shear modulus for all pairings of 3, 6, and 10 mg/ml gels is significantly different ($p<0.05$). These results are plotted along with shear modulus measurements of RAD16-I previously published by Sieminski et al. [40]. The high level of agreement of these two sets of results demonstrates that estimating an elastic shear modulus from the microindentation loading curve gives a result consistent with rheometry in these gels in spite of some inelastic behavior. The elastic assumption is also supported by Sieminski's finding that the storage modulus is more than 6 times the loss modulus in RAD16-I gels at the concentrations we examined. Furthermore, we found that changing the

microindentation loading rate from 5 to 25 μm/s did not significantly change the mean measured shear modulus (p=0.46, not shown).

3.3.5 Varied filament length shows no effect on the stiffness of RAD16-I gels

We have demonstrated how the length of RAD16-I filaments can be consistently controlled by sonication and regrowth. We used this technique to form gels from solutions of shorter or longer RAD16-I filaments. Gels designated as "short" are formed from peptide solutions immediately after sonication, while gels designated as "long" are formed from peptide solutions that have been incubated for 24 hours for filament regrowth. The "short" and "long" designations are expected to correspond to a mean filament length of ~120 nm and ~540 nm, respectively, in RAD16-I (Figure 3.2). Surprisingly, this method of varying filament length showed no significant effect on the shear modulus of peptide gels (Figure 3.7).

3.3.6 Glutaraldehyde treatment increases the stiffness of KLD-12 gels, and varied filament length shows no effect

To examine whether cross-linking of filaments has an effect on gel stiffness, we treated KLD-12 gels with 1% glutaraldehyde for 24 hours. (KLD-12 contains lysine residues, whose amines may be cross-linked by aldehydes; these are lacking in RAD16-I). We also used the same sonication-and-regrowth procedure to test the effect of filament length and the combined effects of filament length and cross-linking on KLD-12.

Glutaraldehyde treatment increased stiffness about 3.5-fold over KLD-12 gels kept in saline solution. However, no significant difference in shear modulus was observed between KLD-12 gels made from recently sonicated ("short") or incubated ("long") peptide solutions, either with or without glutaraldehyde (Figure 3.7).

3.4 Discussion

Short peptides that assemble to form amyloid fibers and macroscopic gels have been extensively studied over the last two decades for use in tissue engineering [65, 90, 91], bioactive molecule delivery [43], and environmentally responsive sensors [56]. Zhang has demonstrated that new self-assembling peptides can readily be designed [96] by mimicking the distinctive charge pattern of the peptide EAK16 ($[AEAEAKAK]_2$), originally observed in yeast zuotin protein [22]. These various peptides follow a similar pattern in their self-assembly. Stable filaments with a β-sheet structure (amyloids) form and persist even at extremes of temperature and pH [35]. In strongly acidic conditions, protonation of acidic side chains gives the peptide filaments a self-repulsive net positive charge, but when the charge is neutralized by raising the pH or shielded by adding electrolytes, peptide filaments aggregate to form stable macroscopic gels [37].

Considerable attention has been given to the structure and mechanical behavior of these materials, from the molecular to the bulk length scales. Filaments with a width corresponding to one peptide length (consistent with a β-sheet structure) have been observed by TEM [32, 97] and AFM [98, 99], and the dominance of a β-sheet secondary structure has been demonstrated by circular dichroism [35]. Work has been done to systematically vary the peptide sequence and examine whether the bulk modulus changes with various factors including identity of hydrophobic amino acids, identity of charged amino acids, peptide length [39], and the period of repetition of the pattern of charge in the oligopeptide sequence [40]. (Only the last two of these factors were shown to be significant.) Molecular dynamics simulations have been used to observe the mechanical properties of individual filaments [59] and the strength of interactions between filaments

[100], and experimental techniques are available to measure the bending stiffness (via persistence length) of filaments [101] and the mechanical properties of bulk gels [40, 42].

But in spite of the high level of attention devoted to self-assembling oligopeptide gels, questions remain about their microscopic structure and its effect on a gel's mechanical properties, and no general paradigm exists to explain their mechanical behavior. In particular, it is unclear how filaments are arranged with respect to one another in a gel. Electron microscopy techniques have suggested that filaments tend to bundle together into larger fibers [40, 102], but the internal structure of these fibers has remained a mystery.

With clear structural data lacking, it has sometimes been assumed that filaments align in parallel into dense bundles of many filaments [36, 42, 100]. A gel formed from such dense bundles lends itself to cellular solids analysis, in which a typical unit cell is considered as a framework of elastic (Euler-Bernouli) beams, and simple scaling arguments relate loads and displacements of a unit cell to bulk stress and strain [10, 83].

However, as we noted in previous work [100], when the cellular solids model is applied to peptide gels it overestimates bulk stiffness by a factor of about 1000. In that study we asked whether free slip between bundled filaments could account for this discrepancy and examined the shear forces between sliding filaments using molecular dynamics simulations and coarse-grained modeling. We concluded that if filaments were tightly packed their resistance to shear loads would be substantial, contrary to the free slip assumption, and we suggested that fibrillar packing may be somewhat disordered. Further evidence against tightly packed filament bundles comes from the observation that

the apparent volume of filament bundles exceeds by many times the volume of peptide present [40].

We present here for the first time thin-section TEM images of RAD16-I and KLD-12 gels embedded in resin (Figure 3.3). In contrast to the apparently dense filament bundles observed by other electron microscopy techniques [40, 102], these images show neighboring filaments to be individually distinguishable and generally not aligned, and with considerable void space present between filaments. To the extent that filament bundles are present, they might be better thought of as loosely woven strands of yarn rather than Euler-Bernouli elastic beams. Also present in these TEM images are globular structures of varying size up to 200 nm in diameter. Similar structures are also observable by AFM and have been reported by others for RAD16-I [99, 103].

In light of these new results that suggest a gel is made up of loosely interacting individual filaments, a model for semiflexible biopolymer networks introduced by MacKintosh et al. [12] may be useful to relate the mechanical properties of individual filaments to bulk properties. This model applies to solutions of filaments whose persistence length is much greater than the characteristic spacing of interactions with other filaments, consistent with a solution of β-sheet fibers with a persistence length on the order of microns [59, 101] and a mesh size on the order of 100-300 nm. The biopolymers model predicts the bulk storage modulus for gels that are not densely cross-linked to be of the form in Equation 3.2.

$$G' \sim \kappa(\kappa / k_B T)^{2/5} (aC_a)^{11/5} \tag{3.2}$$

G' is the shear storage modulus, κ is the bending stiffness, $k_B T$ is the ambient thermal energy, a is the filament length per monomer, and C_a is the concentration. The

bending modulus for RAD16-I or KLD-12 can be reasonably estimated at 1×10^{-26} N·m^2 based on simulations [59] and experiments [101] with other β-sheet-forming oligopeptides. The thermal energy k_BT at room temperature is 4.11×10^{-21} J. The filament length per monomer a is 2.4 Å, given that each filament contains two β-sheets in contact on their hydrophobic surface [59, 104] and the spacing between β-strand monomers is 4.8 Å. The concentration of 10 mg/ml can be expressed as 5.84 mol/m^3 given a molecular weight of 1712 g/mol. The resulting estimate of G' is about 40 kPa, roughly 10× higher than our measurements of G=4.7 kPa for RAD16-I and 1.9 kPa for KLD-12. (Shear modulus G is comparable to storage modulus G' in an elastic gel.) Note that this is only a rough estimate, as the scaling relationship of Equation 3.2 has an undetermined prefactor. The biopolymers model [12] predicts $G'\sim C_a^{11/5}$, while Gibson and Ashby's model [10] predicts a scaling of C_a^2. Using data from the current study (Figure 3.5), a linear fit to a log-log plot of G versus C_a gives an estimate of $G\sim C_a^{1.62}$. Sieminski's rheometry measurements give $G'\sim C_a^{2.53}$ for RAD16-I and $G'\sim C_a^{2.12}$ for a similar self-assembling peptide RAD16-II [40]. In both studies, variability in results is great enough to make precise determination of the relationship between G' and C_a difficult.

Note that the MacKintosh biopolymers model does not account for the inhomogeneous distribution of peptide filaments observed in Figure 3.3, but it nevertheless may be a useful starting point. Also, while the basis of the MacKintosh model is dampening of thermal fluctuations in filaments, other work predicts that under certain conditions thermal effects are negligible. Computational simulations of polymer networks by Kim et al. suggest that thermal fluctuations are unimportant when persistence length is equal to or greater than the cross-linking distance (or entanglement

length) [105]. In the case of self-assembling peptide gels, persistence length l_p is a few microns, while the MacKintosh estimate of entanglement length $l_e \sim (\kappa/k_BT)^{1/5}(aC_a)^{-2/5}$ [12] gives an estimate of about 500 nm, such that $l_p > l_e$. Kim's work would suggest that thermal fluctuations are negligible in this case, and that another model may be appropriate to account for storage of strain energy in non-entropic forms such as filament bending.

We have already examined one such model in chapter 2, the cellular solids model of Gibson and Ashby [10], and found our initial estimates of stiffness to be in poor agreement, overestimating experimental results. Let us revisit this model with the new structural data obtained by thin-section TEM. In these images it appears gels are formed from entanglements of individual filaments 2 thick and 6 nm wide rather than 30-nm-diameter bundles of filaments. The mesh size again appears to be in the range of 100-300 nm, and we again estimate the filament tensile modulus at 15 GPa as for RAD16-II [59]. We adapt Equation 2.8 for a rectangular beam such that

$$E_b \sim \frac{IE}{L^4} \sim \frac{bh^3}{L^4} E_f \tag{3.3}$$

where b and h are the long and narrow dimensions of the cross-section. Depending the mesh size used, this gives estimates of bulk Young's modulus from about 10 to 1000 Pa. (The result is sensitive to L due to the 4th power dependence.) The upper end of this range approaches the measured peptide gel stiffness (G = 2-7 kPa, Figure 3.7) and agrees with results about as well as the MacKintosh model. It is impossible to immediately rule out one model or the other as invalid based on these comparisons.

One of our aims in doing this research was to develop strategies for controlling the stiffness of peptide gels. Cross-linking has been effective for increasing the stiffness

of other hydrogels such as collagen [18], but strategies for cross-linking self-assembling peptide gels using biotin and strepavidin or factor XIIIa transglutaminase did not significantly change the stiffness of peptide gels. Factor XIIIa, which catalyzes cross-links between glutamine and lysine, was able to link a lysine-containing peptide to the glutamines of self-assembling peptide Q11 (Ac-QQKFQFQFEQQ-Am), but failed to form cross-links between Q11 molecules; it is not clear why [44]. Introducing streptavidin to biotinylated RAD16-II (Biotin-G_6-$[RARADADA]_2$-Am) peptide gels also failed to increase gel stiffness [68], although this may have been due to the short time allowed for diffusion of streptavidin into the gel (2 h in a gel 900 μm thick). To test again whether cross-linking could be an effective strategy, we instead used a small, non-specific cross-linking agent, glutaraldehyde (100 Da), to link the amines in the lysine residues of the peptide KLD-12. We were able to demonstrate for the first time the effectiveness of cross-linking in stiffening self-assembling peptide gels, with a 3.5-fold increase in bulk gel stiffness after 24 h of treatment with 1% glutaraldehyde (Figure 3.7).

A second form of the biopolymers model of MacKintosh et al. which predicts the behavior of densely cross-linked gels is given in Equation 3.4.

$$G' \sim \kappa(\kappa / k_B T)^{2/5} (aC_a)^{11/5} \tag{3.4}$$

This model predicts a 30,000× increase in G' after dense cross-linking, in clear disagreement with the modest 3.5× increase that we observed. Our cross-linked KLD-12 gels reached a shear stiffness of about 7 kPa, which still falls in the range of about 1-10 kPa observed for other self-assembling peptide gels (e.g. [39, 40]). This suggests an upper limit of stiffness that may be determined by a physical phenomenon not accounted

for in the MacKintosh model, but further work is required to determine if this is the case and what might cause such an upper limit in stiffness.

We also examined the effect of filament length on bulk stiffness of peptide gels. Yokoi et al, have previously demonstrated how RAD16-I filaments can be broken into short fragments by sonication and allowed to regrow over time by incubating at neutral pH [98]. In order to form dense solutions of peptide with varied filament length before inducing gelation, we applied this sonication-and-regrowth technique to acidic solutions (~pH 2) of 10-mg/ml RAD16-I prior to gelation. We demonstrated that RAD16-I peptide filaments could be broken to about 120 nm in length by sonication and allowed to regrow to a mean length of 540 nm over a period of 24 hours. We observed a linear growth profile over the full 24 hour period. Linear growth is consistent with end-to-end joining of filaments in a second-order kinetic reaction, where the free filament ends are treated as the reactive species [106]. However, Yokoi observed rapid initial growth in filament length followed by a slowing growth rate. At present we can only speculate about the reason for this difference. It may be caused by to the different pH in the two experiments, and the resulting difference in filament charge (neutral for Yokoi, highly charged in our study). Another possibility is that Yokoi's sonication broke filaments into monomeric form, such that at early time points growth was dominated by a rapid nucleation-polymerization process, later slowing to end-to-end growth as the monomer was used up.

With mean filament lengths in our experiment ranging from 120 to 540 nm, we anticipated a significant change in gel stiffness. Contrary to our expectation, forming gels from solutions with varied filament length produced no effect on bulk stiffness of RAD16-I, KLD-12, or glutaraldehyde-treated KLD-12. One explanation to consider is

that the range of filament lengths examined (about 120-540 nm) is large compared to the mesh size, making bulk stiffness relatively insensitive to filament length (as demonstrated in actin gels [107]). However, this explanation is contradicted by our thin-section TEM images (Fig 3) and other imaging studies [40, 102] which indicate a mesh size of ~100-300 nm, on the order of our mean filament length, such that one would expect bulk mechanical properties to be sensitive to changes in filament length. Another possibility is that the filament length in the peptide solutions from which gels are formed does not equate to filament length within the assembled gels. If the growth rate of filaments at neutral pH is high enough relative to growth at low pH, then mean filament length could increase significantly during gel formation. The results of Yokoi et al. suggest that this may be the case, as they observe growth to filaments of over 500 nm within 3 hours for RAD16-I [98]. Since there is currently no known method to measure filament length after filaments have assembled to form gels, we cannot rule out this possibility.

3.5 Conclusion

We have demonstrated that microindentation is an effective technique for characterizing self-assembling peptide gels using small-volume (~12 μl) samples, and that estimating the shear modulus by fitting Hertz law to force-indentation data gives results in agreement with rheometry. We used this technique to examine the effects of 1) cross-linking peptide gels with glutaraldehyde, for a 3.5-fold increase in shear modulus, and 2) forming gels from varied lengths of filaments, which had no effect. Thin-section TEM images of peptide gels have provided a higher resolution view of the gel microstructure than previous methods, giving evidence that bundled filaments do not pack densely but rather as a loose mat of crossed filaments. Demonstrated strategies for

varying gel stiffness now include varying peptide concentration and introducing cross-links between filaments.

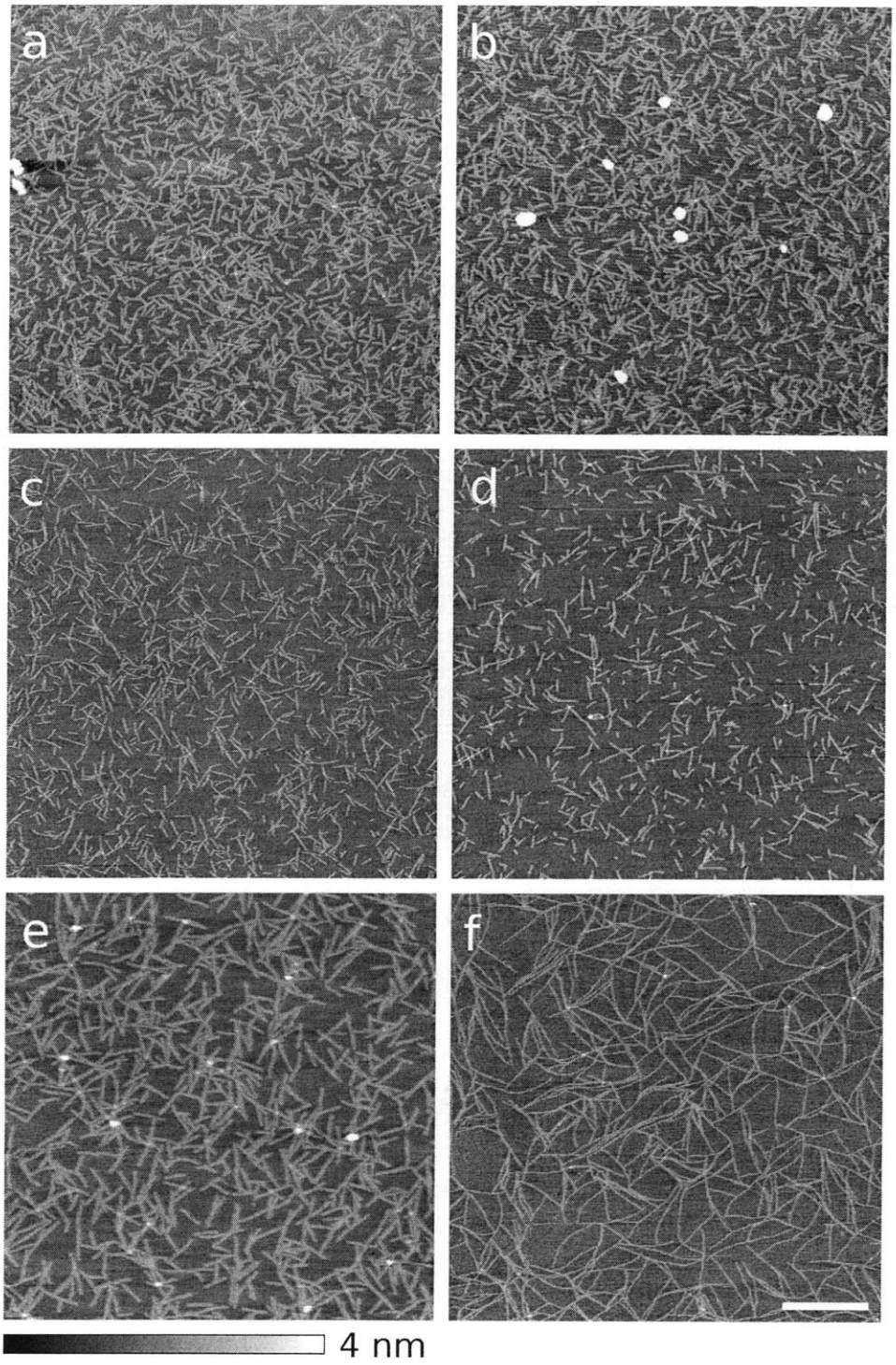

Figure 3.1. AFM scans of RAD16-I deposited on mica following incubation of (a) 0 h, (b) 1 h, (c) 2 h, (d) 4 h, (e) 8 h, and (f) 24 h after sonication. Immediately after sonication RAD16-I peptide consists of many short filaments about 100 nm in length. Over time, the total number of deposited filaments gradually decreases but the average filament length increases correspondingly, with filaments ranging from a few hundred nm to about 1.5 μm. Scale bar is 1 μm.

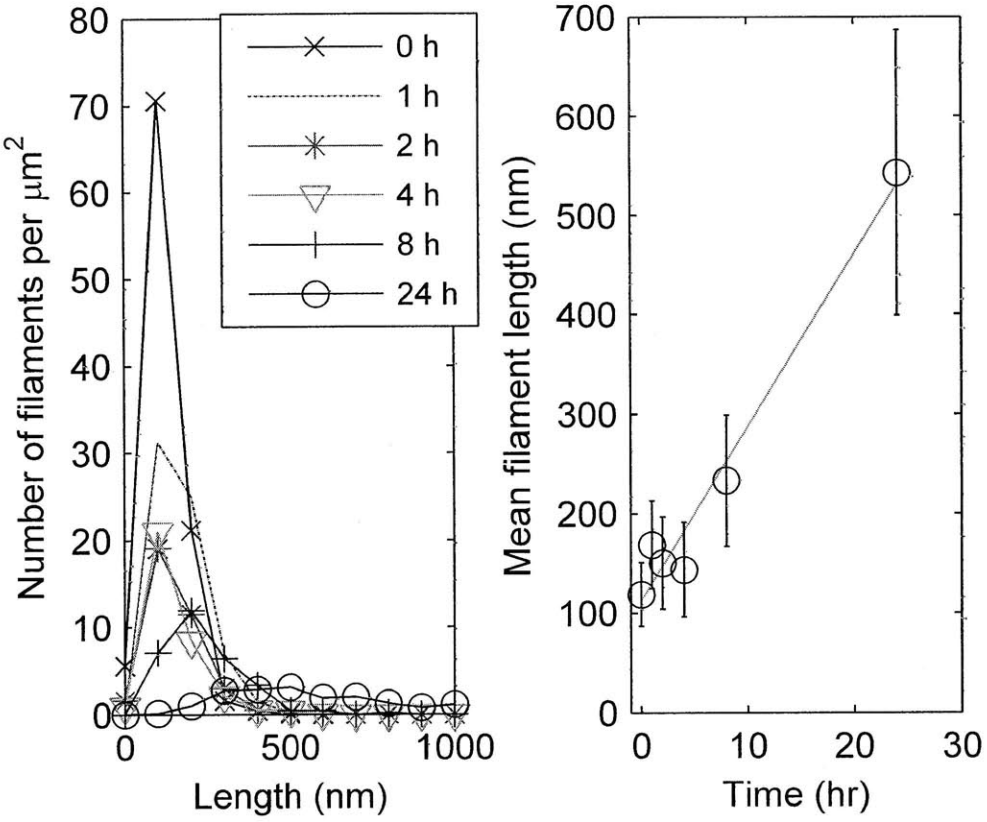

Figure 3.2. Filament lengths were measured from AFM scans of RAD16-I prepared with varied time for filament regrowth after sonication. (a) A histogram shows the number of filaments of a given length range deposited per unit area. Filaments appear to join together over time, creating a smaller number of filaments but with greater average length. (b) The mean length and standard deviation of the filament populations are plotted, revealing a growth trend that is approximately linear over the time examined, with an initial filament length of 120 nm and a statistically significant ($p<0.01$) growth rate of 17 nm/h.

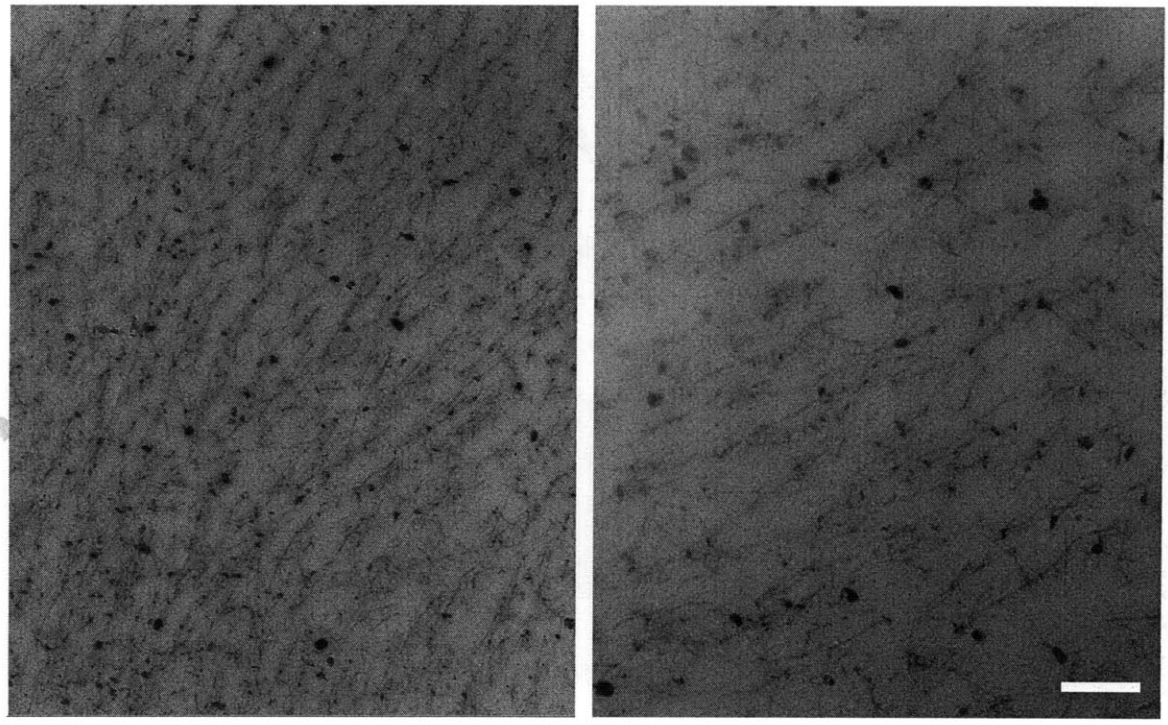

Figure 3.3. Thin-section TEM images reveal that both RAD16-I (left) and KLD-12 (right) gels are made up of loosely associated filaments rather than tightly packed filament bundles. Nonfibrillar, globular particles up to 200 nm in diameter make up a significant fraction of the stained material in the images. Scale bar is 500 nm.

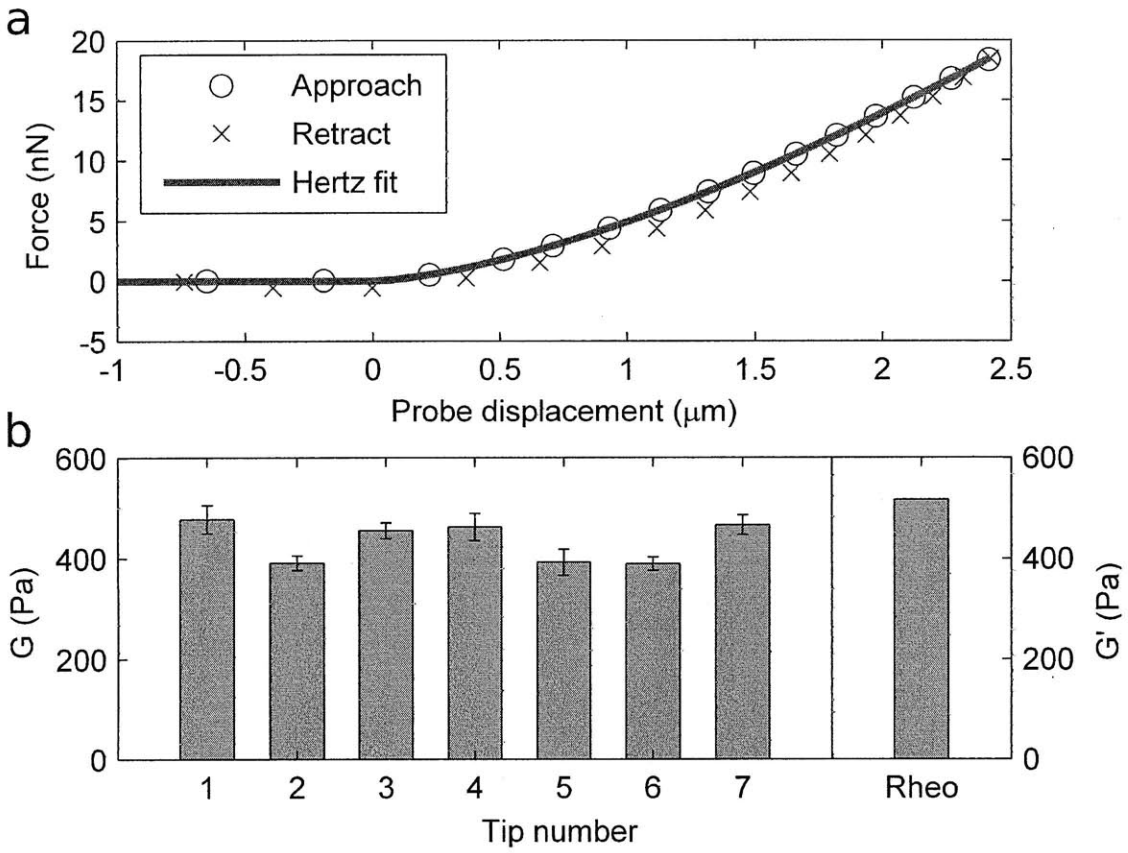

Figure 3.4. A polyacrylamide gel was used to characterize the microindentation method. (a) A typical force-displacement curve including approach and retraction exhibits little hysteresis. A best fit of the Hertz model (Equation 3.1) is also shown. (b) Rheometric measurement of polyacrylamide gel gave a storage modulus of 517 Pa at 1 Hz, with little variation from 0.1-10 Hz. (not shown). Measurement of the shear modulus by microindentation was repeated with 7 AFM tips modified by attaching a 10-μm diameter bead. The mean shear modulus was 434 Pa in rough agreement with rheometry. Standard deviation of mean shear modulus measurements between tips was about 10% of the mean, and standard deviation of multiple measurements at distinct locations on one gel with the same tip was about 5%.

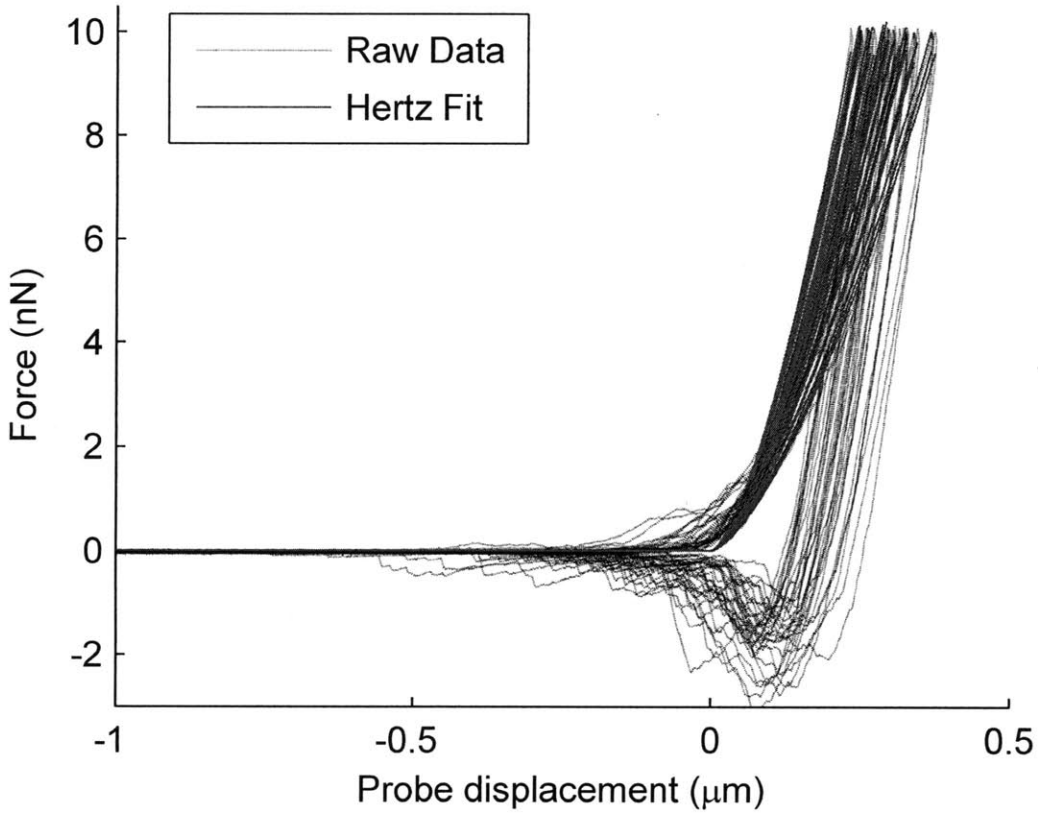

Figure 3.5. Multiple force-displacement curves taken from different locations on one gel (RAD16-I, 10 mg/ml) are shown, along with a best fit of the Hertz model (Equation 3.1) to each approach curve. Some hysteresis is evident, with retraction curves showing an adhesion force of about 1 nN before release.

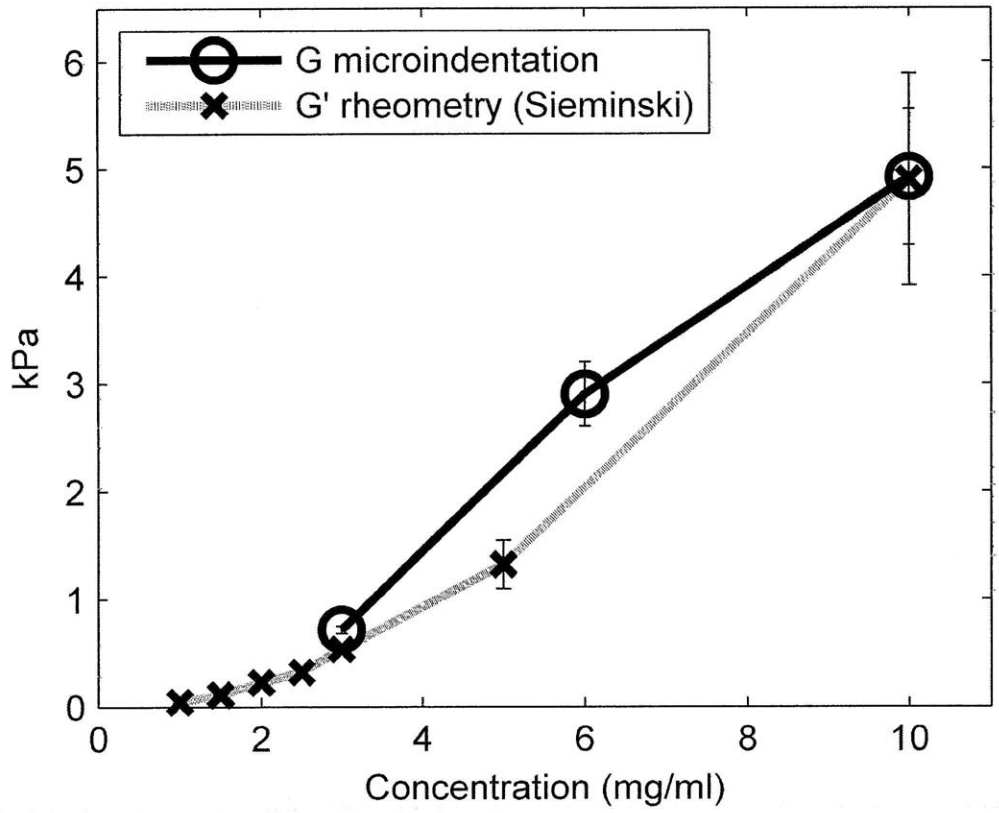

Figure 3.6. The shear moduli of RAD16-I gels were measured by microindentation on 3, 6, and 10 mg/ml gels. Mean shear modulus increased almost 7-fold as gel concentration was increased from 3 to 10 mg/ml. Each data point represents 3 gels, with 20 measurements per gel. Bars show standard error (n=3). Results are in good agreement with storage moduli measured by rheometry published by Sieminski et al. [40].

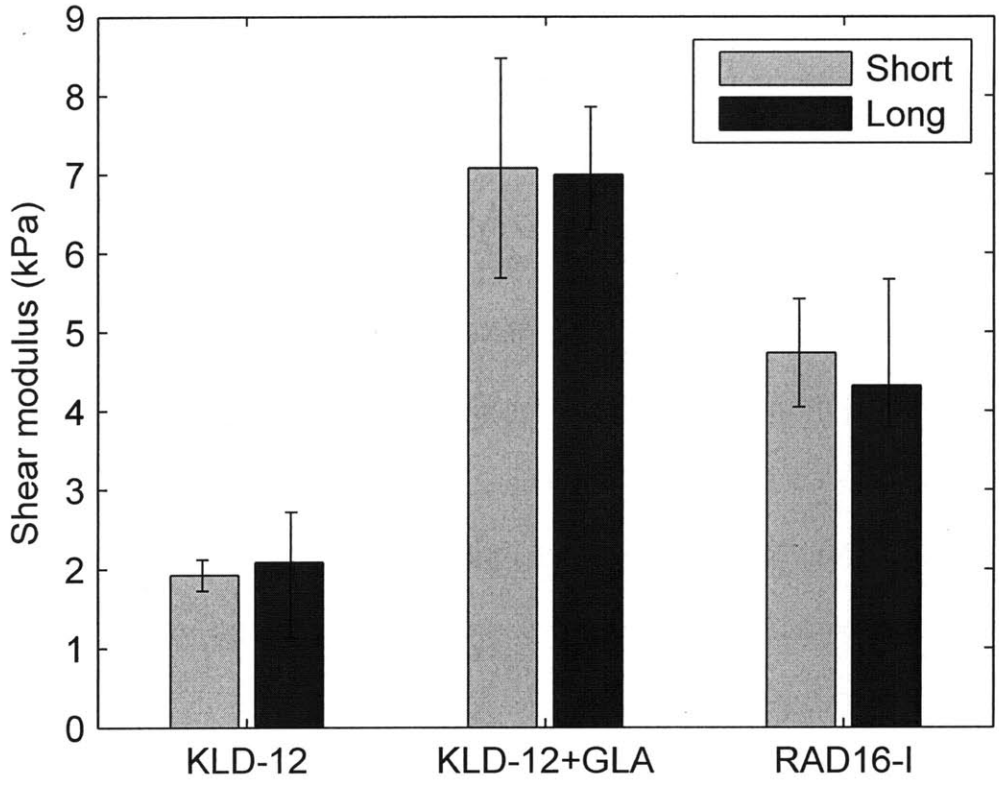

Figure 3.7. Treating KLD-12 peptide gels with glutaraldehyde (GLA) significantly increased shear modulus for both short (p=.028) and long (p=.020) preparations. No significant difference in shear modulus was observed between short and long preparations in KLD-12, glutaraldehyde-treated KLD-12, or RAD16-I gels. Bars show standard error (n=3).

Chapter 4 Other applications of microindentation for self-assembling peptide gels*

4.1 Introduction and background

In developing the microindentation technique for mechanical characterization of gels, we sought to make a simple, standard method that could be easily used for many different hydrogels. In this chapter we will discuss two studies where we applied this technique to characterize self-assembling peptide gels that were of particular interest to collaborating researchers.

4.1.1 Functionalized scaffolds with MMP-cleavable cross-links and laminin-derived binding motifs

Yoshi Kumada and Shuguang Zhang.have recently begun investigating materials designed to promote the migration of periodontal ligament fibroblasts, with potential applications in periodontal tissue reconstruction. Two new self-assembling peptides called VEVK9 and VEVK12 were designed for this purpose. VEVK9 was also synthesized with attached binding motifs or with a sequence cleavable by matrix metalloproteases (MMPs). The peptide sequences created for this study are described in Table 4.1 and illustrated in Figure 4.1.

The three incorporated binding motifs include one with the RGD sequence, well known for its role as a ligand for integrin binding, and two adhesion motifs found in laminin (YIGSR and IKVAV). The importance of these motifs for adhesion, migration, proliferation, and differentiation has been demonstrated [108, 109]. An MMP-cleavable sequence (PVGLIG) was included to facilitate cell migration by allowing partial degradation of the gel with the secretion of MMPs by migrating cells. The same

* Material from this chapter is included in an article that was submitted for publication in a peer-reviewed journal. Yoshi Kumada, Nathan A. Hammond, and Shuguang Zhang, 2010.

sequence has been incorporated into cross-links in RAD16-I gels [89], and another MMP-cleavable sequence was previously used in PEG gels and shown to accelerate cell migration in vitro and bone healing in vivo [110].

Gels were prepared either as pure VEVK9 or VEVK12, or as a mixture of either VEVK9 or VEVK12 with one or more of the functionalized peptides. Gel formulations are described in Table 4.2. Differing behavior of fibroblasts on this set of materials can give insight into the role of binding motifs and the potential for facilitating migration with MMP-cleavable crosslinks.

Mechanical characterization of the various gel formulations was an essential part of this work, since gel stiffness can also play a role in cell migration [111], and this effect had to be quantified and isolated from the effects of the binding motifs and MMP-cleavable cross-links.

4.1.2 Peptide gels with fibronectin-derived binding motifs and biotin-streptavidin crosslinks for tethered growth factor

A recently published work from the Linda Griffith laboratory by Geeta Mehta, Courtney Williams, and others [88] explores different forms of stimulation of EGFR in rat hepatocytes cultured in vitro. This study used RAD16-I gels functionalized with fibronectin-derived binding motifs (PRGDSGYRGDS and WQPPRARITGY) known to be active in hepatocyte adhesion. The gels were also functionalized with biotin such that biotinylated EGF could be attached to the matrix with streptavidin, mimicking stimulation of EGFR by the matrix protein tenascin-C, which presents EGF-like repeats. These peptide sequences are displayed in Table 4.3, and the various gel formulations used are in Table 4.4. Since RAD16-I does not have any known inherent signaling activity, this system gives total control over the presence and concentration of binding

motifs in the matrix, and also enables comparison of EGF presented in bound or soluble forms. However, since modifying the peptides may alter the stiffness of the gels they form, and since gel stiffness can play an important role in hepatocyte behavior (for example, differences are observed between culture on a collagen film or a collagen gel [112]), it was important to characterize the mechanical properties of the gel formulations used in this study.

4.2 Methods

4.2.1 AFM imaging of peptide filaments

Peptide solution was diluted to 0.01 mg/ml in 0.01 M HCl. The diluted solution was shaken vigorously for 20 seconds before 5 µl peptide solution was pipetted onto a freshly cleaved mica surface. After 20 seconds, the mica was rinsed with 500 µl of deionized water and wicked dry with tissue paper. Peptide solutions were allowed to dry and were scanned within 24 hours using a Nascatec (Kassel, Germany) model NST-FM probe (70 kHz) on a Veeco Nanoscope IIIa Multimode atomic force microscope (Plainview, NY) in tapping mode.

4.2.2 Measurement of the stiffness of peptide gels

Gel preparation, microindentation testing, data processing, and statistical analysis were carried out as described in Chapter 3. The only modification is that Hertz law is here expressed in terms of Young's modulus instead of shear modulus. We use the relation $E = 2G(1 + \upsilon)$, valid for isotropic materials, to rewrite Equation 3.1 in this form:

$$F = \frac{4E}{3(1-\nu^2)} R^{\frac{1}{2}} \delta^{\frac{3}{2}} \tag{4.1}$$

The least-squares best fit of force-displacement data from microindentation described in Chapter 3 now gives an estimate of Young's modulus E.

4.3 Results

AFM scans confirmed the ability of VEVK9 and VEVK12 to form filaments similar to those observed in RAD16-I and other similar self-assembling peptides. VEVK12 formed filaments that appeared more curved and irregular (Figure 4.2) than typical self-assembling oligopeptides, such as the RAD16-I filaments reported in Chapter 3. In pure VEVK9, no filaments were observable by AFM on the mica surface, although the formation of a gel with elastic properties suggests that filaments of VEVK9 do form in solution. When VEVK9 is mixed with vPRG and vPVG (8:1:1), two populations of filaments are observed (Figure 4.2). The first is relatively thin and flexible. The second is thicker and straighter. These thicker structure may result from two filaments that have joined together in the presence of MMP-cleavable cross-linkers.

Mechanical characterization of VEVK9 and VEVK12 gels reveals that VEVK12 is stiffer (5 kPa) than VEVK9 (0.94 kPa) at the same mass concentration (Figures 4.3, 4.4). The addition of MMP-cleavable cross-linkers and any of the functionalized peptides generally increases the stiffness of both gels. Among the formulations examined, the greatest increase in stiffness comes with the addition of vIKV (laminin motif) and vPVG (cross-linker) in both VEVK9 (3.8 kPa) and VEVK12.(7.5 kPa).

While the addition of binding motifs and MMP-cleavable cross-linkers increases the stiffness of both VEVK9 and VEVK12, it is interesting to note that the increases is much more pronounced in VEVK9.

Mechanical characterization of the modified RAD16-I gels for hepatocyte culture showed that neither the addition of biotinylated peptide nor of biotinylated peptide plus the RGD-containing sequence changed the gel stiffness significantly. However, when the heparin-binding motif was added in addition to these (formulation r4, Table 4.4), the

Young's modulus of the gel fell by half, from 10 kPa to less than 5 kPa (Figure 4.5). It is not clear to what part of this decrease is caused by the heparin binding motif itself and what part may be caused by a smaller mass fraction (70%) of non-functionalized self-assembling peptide in this formulation (RAD16-I). The reduced stiffness of this gel formulation should be considered in interpreting the results of Mehta's study [88]. Of all the formulations of synthetic peptide, significant DNA synthesis was only observed in the gels with RGD, heparin-binding domain, and tethered EGF. The fact that this gel formulation unexpectedly had a reduced stiffness complicates the comparison with results from other gels.

4.4 Discussion and Conclusion

We have demonstrated that microindentation can serve as a useful tool for characterizing new self-assembling peptide gels with a range of properties. Many of the gels we examined contained functional groups added to a self-assembling peptide. Taken together, these results demonstrate that the influence of these functional groups on the mechanical properties of peptide gels is quite complex. They may either increase or decrease the gel stiffness, and the behavior is not predictable simply by the length of the added functional sequence. Since the impact of functionalized peptides on the mechanical properties of a gel can be significant and is thus far unpredictable, it is recommended to measure the stiffness of functionalized peptide gels whenever variations in gel stiffness could influence the experimental results in a way that would obscure the effects of other variables.

Table 4.1
Self-assembling peptide sequences with laminin-derived motifs and an MMP-cleavable cross-linker

Name	Sequence	Description
VEVK9	Ac-VEVKVEVKV-NH_2	Self-assembling peptide
vPRG	Ac-VEVKVEVKV-GPRGDSGYRGDS-NH_2	2-unit RGD motifs
vYIG	Ac-VEVKVEVKV-GYIGSR-NH_2	Laminin cell adhesion motif (YIGSR)
vIKV	Ac-VEVKVEVKV-GIKVAV-NH_2	Laminin cell adhesion motif (IKVAV)
vPVG	Ac-VEVK-GPVGLIG-VEVK-NH_2	MMP-cleavable cross-linker
VEVK12	Ac-VEVKVEVKVEVK-NH_2	Self-assembling peptide

Table 4.2
Gel formulations for in vitro fibroblast culture

Gel Formulation	Peptides	Ratio
v1	VEVK9	--
v2	VEVK9 + vPVG +vPRG	2:1:1
v3	VEVK9 + vPVG + vIKV	2:1:1
v4	VEVK9 + vPVG + vYIG	2:1:1
v5	VEVK12	--
v6	VEVK12 + vPVG + vPRG	2:1:1
v7	VEVK12 + vPVG + vIKV	2:1:1
v8	VEVK12 + vPVG + vYIG	2:1:1

Table 4.3
Self-assembling peptide sequences with fibronectin-derived motifs and biotin for EGF tethering

Name	Sequence	Description
RAD	Ac-$[RADA]_4$-Am	RADA16-I self-assembling peptide
RGD	Ac-$[RADA]_4$-GPRGDSGYRGDS –Am	RAD16-I with RGD-containing sequence
Bio	Ac-$[RADA]_4$-Biotin-Am	RAD16-I with biotin
HB	Ac-$[RADA]_4$-GGWQPPRARITGY-Am	RAD16-I with heparin binding sequence

Table 4.4
Gel formulations for in vitro hepatocyte culture

Gel Formulation	Peptides	Ratio
r1	RAD	--
r2	RAD + Bio	9:1
r3	RAD + Bio + RGD	8:1:1
r4	RAD + Bio + RGD + HB	7:1:1:1

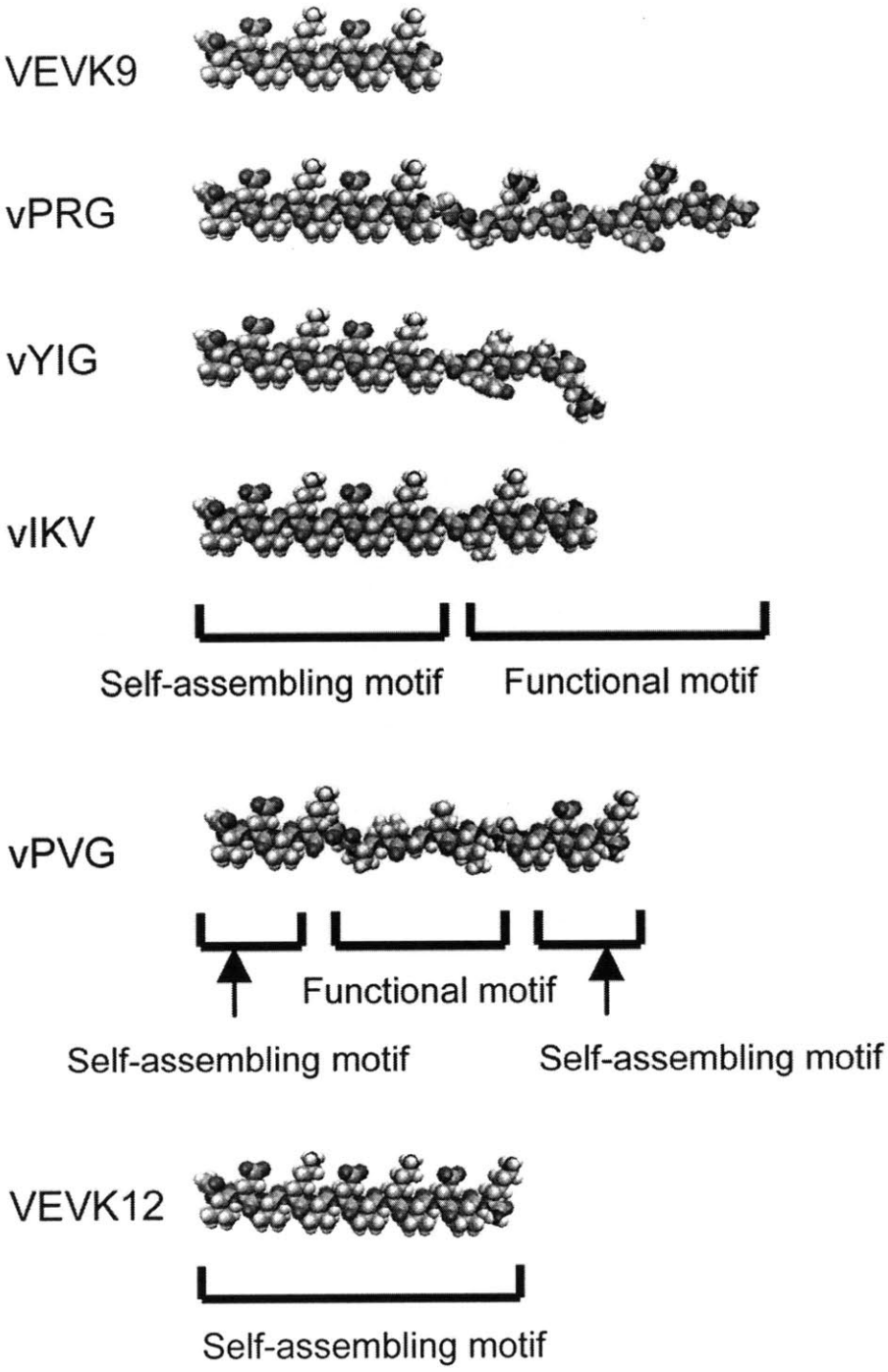

Figure 4.1. Molecular models of the peptides VEVK9, vPRG, vYIG, vIKV, vPVG and VEVK12.

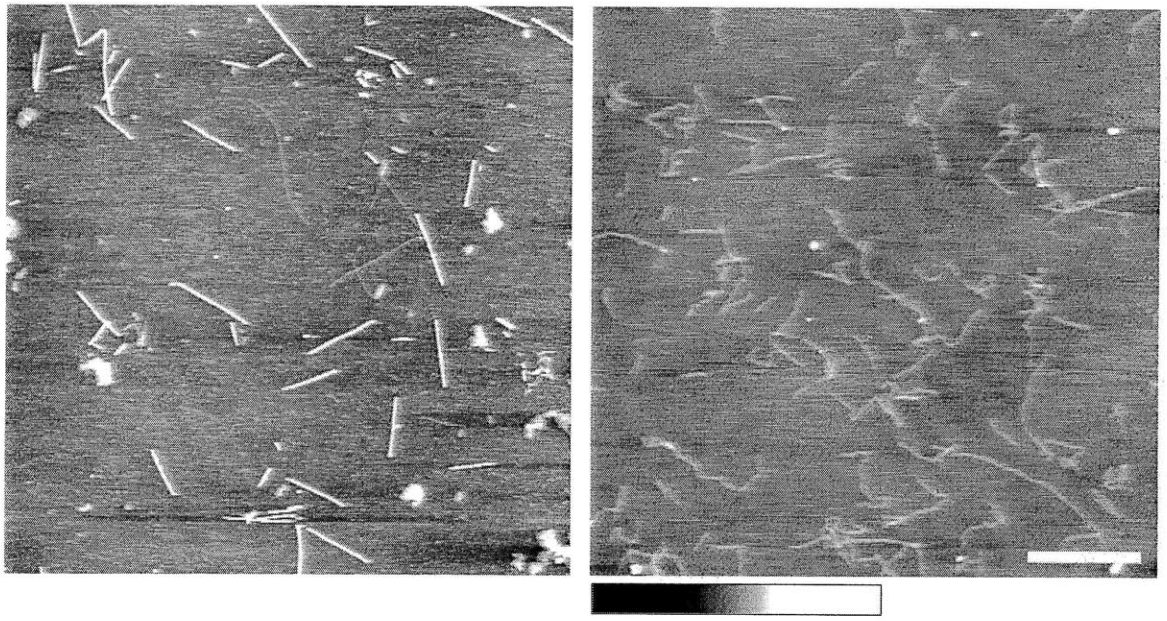

Figure 4.2. (left) VEVK9 mixed with vPRG and vPVG. (right) VEVK12. Scale bar is 1μm. Color bar spans 10 nm.

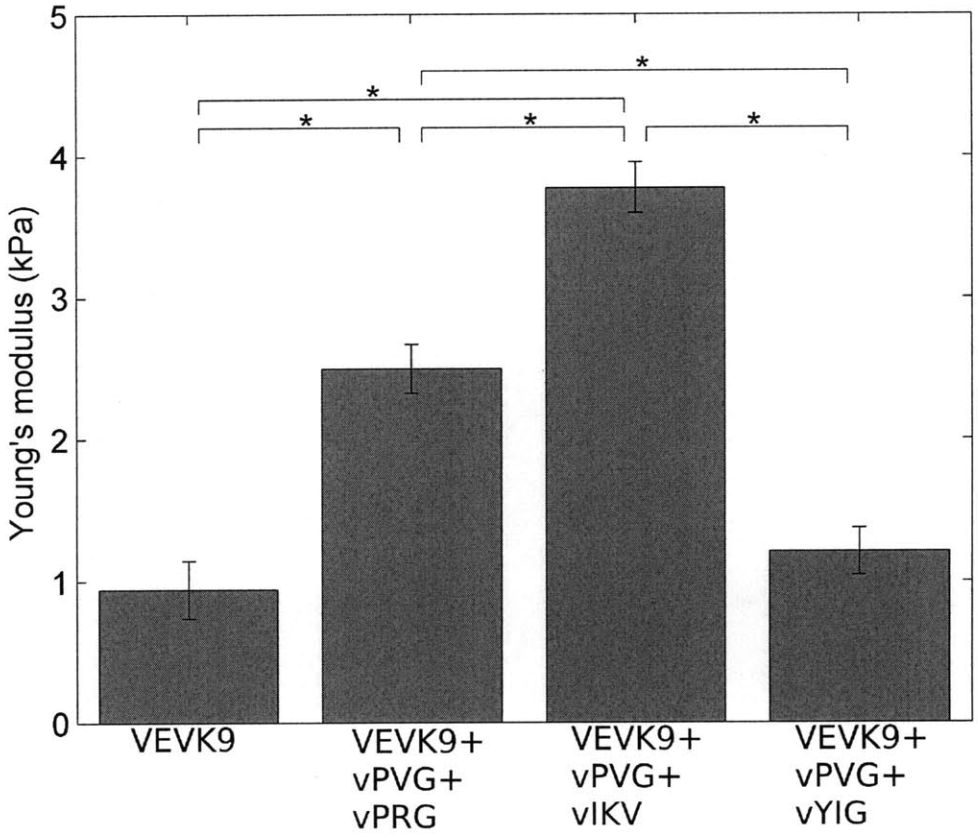

Figure 4.3. Young's modulus of gels formed from VEVK9 and mixtures of VEVK9 with functionalized peptides. Brackets show standard error. Significantly different pairings (p<0.5) are indicated (*).

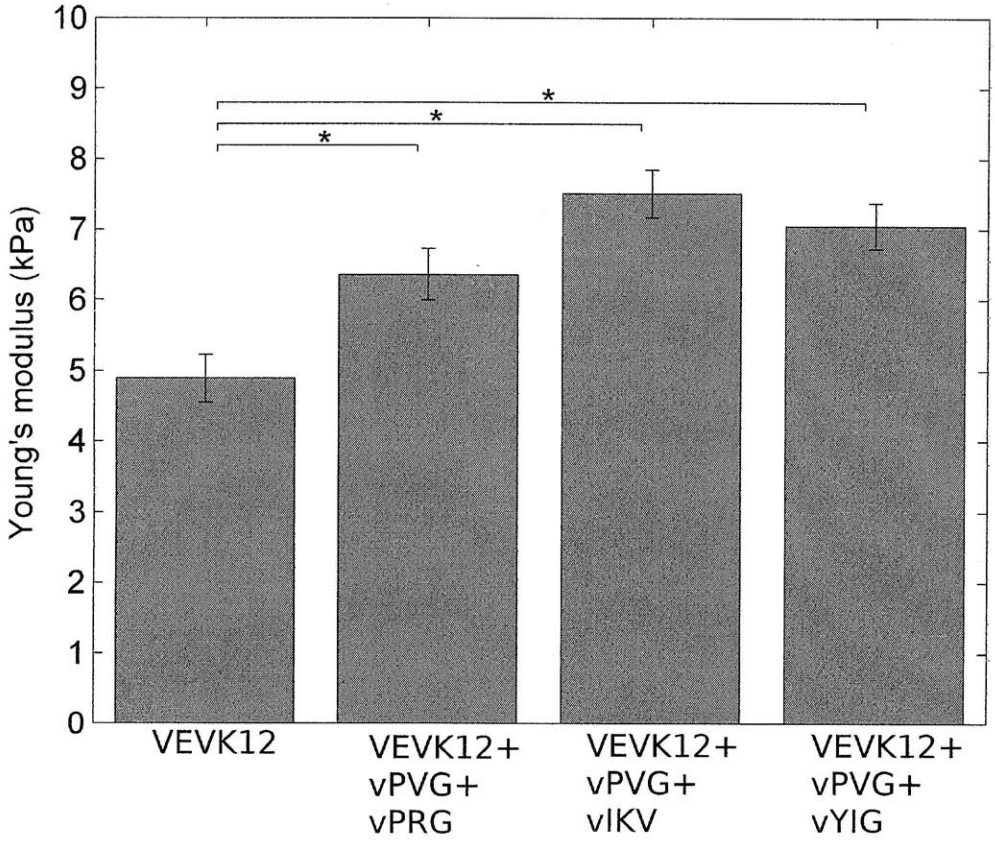

Figure 4.4. Young's modulus of gels formed from VEVK12 and mixtures of VEVK12 with functionalized peptides. Brackets show standard error. Significantly different pairings (p<0.5) are indicated (*).

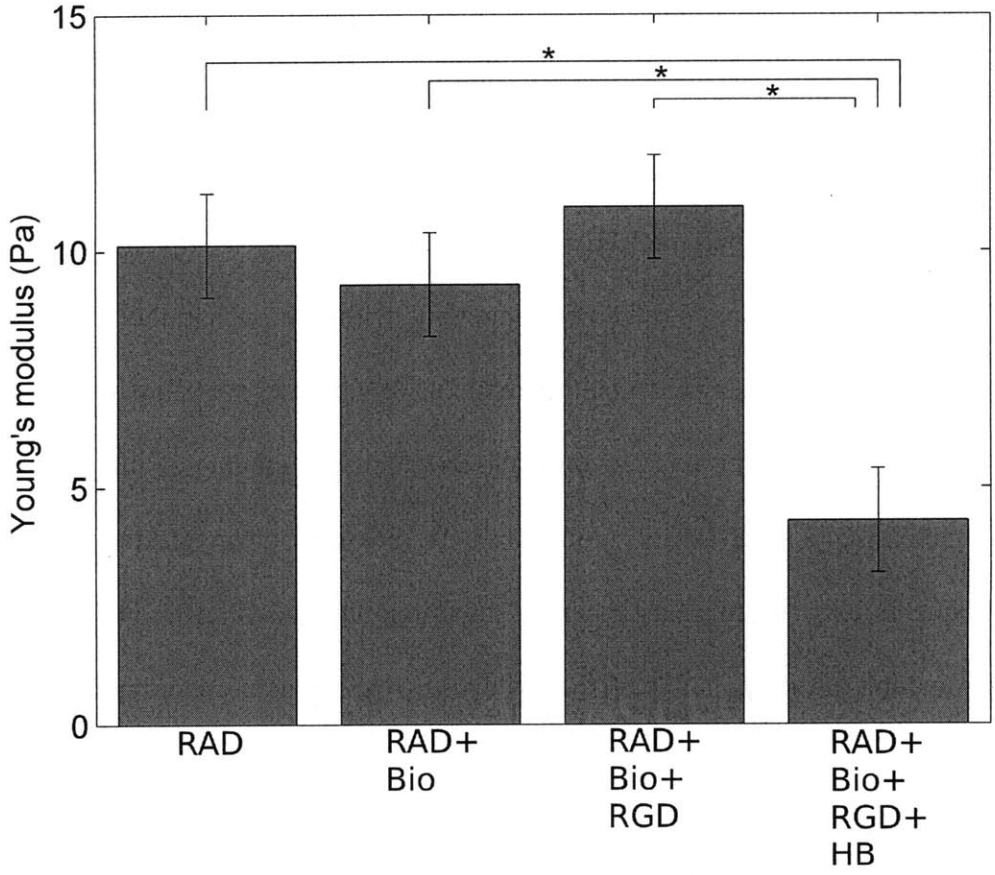

Figure 4.5. Young's modulus of gels formed from RAD and mixtures of RAD with biotinylated and otherwise functionalized peptides. Brackets show standard error. Significantly different pairings (p<0.5) are indicated (*).

Chapter 5 Conclusion

The principal aims of this work were to better understand the mechanisms governing the mechanical behavior of gels formed from self-assembling beta-sheet-forming peptides such as RAD16-I, RAD16-II, and KLD-12, and to work toward the development of mechanically enhanced self-assembling peptide gels. A combined approach of computational and experimental techniques was utilized to achieve these aims.

Molecular dynamics simulations were used to model the mechanical interactions between two peptide filaments of RAD16-II under shear loads. Beneath a threshold stress of about 83 MPa, we observed an elastic regime with a shear modulus of 1.8 GPa. A previous study reported a tensile Young's modulus of 9.5-21 GPa [59], which would correspond to a shear modulus of 3.2-7.0 GPa in an isentropic, incompressible material. Our finding of 1.8 GPa shear modulus indicates a degree of anisotropy in stacked, parallel filaments. Beyond this elastic regime, time to failure was shown to be a stochastic function of the applied load. Shear loads of 183 MPa or less did not cause failure in the 1-ns time span of our simulations, and for higher loads the time to failure decreased with increasing stress.

The dependence of time to failure on applied load indicates that the failure stress observed at the ns time scale is probably much higher than failure stress at a time scale of seconds. To help extend our results to ordinary time scales, we developed a coarse-grained, one-dimensional model of slippage between filaments that captures the behavior observed in the molecular dynamics simulations. The model consists of an elastic chain of particles, each representing one peptide, resting in a periodic function of energy wells that corresponds to the periodic structure of the neighboring filament to which the

modeled filament is adhered. Langevin dynamics simulations with this coarse-grained model led to an estimated the failure strength of about 45 MPa on a time scale of seconds.

These results helped to rule out two hypotheses for why the stiffness of peptide gels is as low as it is. Hypothesis 1) Although filaments form dense bundles with no slippage between filaments, the shear modulus is so low compared to the tensile Young's modulus that these filament bundles have low resistance to bending. This theory is not consistent with the mild anisotropy that we observed. Hypothesis 2) Although filaments form dense bundles, filaments slip freely against each other in shear. This theory is not consistent with the high shear failure strength observed in simulations. One remaining explanation is Hypothesis 3) Filaments do not form dense bundles. Void spaces exist between the filaments such that each filament's bending is governed by its own moment of inertia. (This last result, suggested by modeling, was later found to be consistent with images of gel microstructure.)

A microindentation procedure was developed to measure the Young's modulus of small (~10 μl) samples of gel. Indenter probes were fabricated using atomic force microscopy tips with 10-μm polystyrene beads affixed with glue. This method proved useful in measuring the properties of gels developed by collaborators for tissue engineering applications. First, various formulations of RAD16-I were characterized, with binding motifs for attachment of hepatic cells or biotin for attachment of endothelial growth factor. Second, two new peptides, VEVK9 and VEVK12 were characterized, along with attached binding motifs and an MMP-cleavable cross-linker. These results demonstrate the utility of this method and its applicability to various gels.

Using the microindentation assay, we tested two strategies for increasing the Young's modulus of self-assembling peptide gels. First, we showed that by sonicating solutions of RAD16-I peptide filaments and allowing varied time for the filaments to regrow, we could control the length of peptide filaments over a range of about 100-500 nm. Gels formed from solutions of peptide with varied length, however, showed no change in Young's modulus of the final gel. Second, we used glutaraldehyde to cross-link gels made with the peptide KLD-12, whose lysines are available for cross-linking by glutaraldehyde. This brought a 3.5-fold increase in gel stiffness, the first demonstration that cross-linking can be an effective strategy for altering the mechanical properties of self-assembling peptide gels.

We found that the stiffness of gels measured by this and other methods in the literature are roughly consistent with stiffness estimates made with the biopolymers model of MacKintosh et al., which describes solutions of semi-flexible filaments that interact via non-specific mechanical entanglements [12]. This idea was further supported with transmission electron microscopy of ultra-thin sections of gel embedded in resin. These images gave a detailed view of the internal structure of filament bundles and revealed it to be a disorganized mat of individual filaments with significant void space between them.

Future work

The microindentation methods presented here were used only to measure the elastic properties of peptide gels. It has been noted that similar techniques might be used to study plastic failure [50] and poroelastic behavior [13]. Further developing this technique could provide more detailed information about the mechanical behavior of peptide gels.

Much work remains to be done to understand why different peptide sequences form gels of different stiffness, with variations as large as a factor of 10 [39]. This will require methodical experimental work that goes beyond simple bulk modulus measurements and looks at the observable underlying properties that contribute to bulk material properties. In particular, the persistence length of individual filaments can be measured by AFM of dried filaments or by microscopy of fluorescently tagged dilute peptide filaments. The fraction of material forming non-filamentous structures might be accounted for by first filtering the peptide solution, then measuring the peptide concentration in the remaining material.

Given the limitations of imaging hydrated protein structures with nm resolution, non-imaging techniques that can give insight into the microstructure should also be explored. For example, measuring hydraulic permeability or observing the cut-off size for beads passing through the gels would give some information about the pore size within the gels.

However, it seems that gels formed from ribbon-shaped amyloid peptides have shear moduli that fall mostly within a range of about one order of magnitude. With our new understanding of the structure and mechanical behavior of self-assembling peptide gels, let us ask the question, "How could one make the strongest, stiffest peptide gel possible?" If the MacKintosh model is indeed an accurate description of gel behavior, we can expect gel stiffness to vary as filament bending stiffness to the 1.4 power [12]. Consider that the bending stiffness of the ribbon-shaped filaments of RAD16-I is about 10× greater in the wide direction than in the narrow direction [59]. If peptides could be designed to form filaments with a larger moment of inertia in the weakest bending

direction, bulk gel stiffness could be increased. An example of such a structure is the triple-β-helix domain of the cell puncture needle of the bacteriophage T4 virus [113]. It may be possible to design a similar structure with a triangular or square cross-section based on short synthetic peptides designed with complementary charge patterns that ensure assembly in the desired order. Larger honeycomb or other 2-dimensional cell structures might also be designed. These materials could maintain all the benefits of currently known self-assembling oligopeptides while providing novel microstructures and increased stiffness and strength.

References

1. Ferry, J.D., *Viscoelastic Properties of Polymers.* 3rd ed. 1980, New York: John Wiley & Sons, Inc.
2. Lee, K.Y. and D.J. Mooney, *Hydrogels for Tissue Engineering.* Chemical Reviews, 2001. **101**(7): p. 1869-1880.
3. Kamath, K.R. and K. Park, *Biodegradable hydrogels in drug delivery.* Advanced Drug Delivery Reviews. **11**(1-2): p. 59-84.
4. Qiu, Y. and K. Park, *Environment-sensitive hydrogels for drug delivery.* Advanced Drug Delivery Reviews, 2001. **53**(3): p. 321-339.
5. Lee, S.J. and K. Park, *Synthesis and characterization of sol-gel phase-reversible hydrogels sensitive to glucose.* Journal of Molecular Recognition, 1996. **9**(5-6): p. 549-557.
6. Wichterle, O. and D. Lim, *Hydrophilic Gels for Biological Use.* Nature, 1960. **185**(4706): p. 117-118.
7. Dušek, K. and D. Patterson, *Transition in swollen polymer networks induced by intramolecular condensation.* 1968. p. 1209-1216.
8. Liu, G., et al., *Swelling behaviors and mechanical properties of polymer gel/poly(N -vinyl-2-pyrrolidone) complexes.* Journal of Polymer Research, 2007. **14**(6): p. 461-465.
9. Flory, P.J., *Statistical Mechanics of Chain Molecules.* 1969, New York: Interscience.
10. Gibson, L.J. and M.F. Ashby, *Cellular solids: structure and properties.* 1988, Oxford: Pergamon Press.
11. Stachowiak, A.N., et al., *Bioactive Hydrogels with an Ordered Cellular Structure Combine Interconnected Macroporosity and Robust Mechanical Properties.* Advanced Materials, 2005. **17**(4): p. 399-403.
12. MacKintosh, F.C., J. Käs, and P.A. Janmey, *Elasticity of Semiflexible Biopolymer Networks.* Physical Review Letters, 1995. **75**(24): p. 4425.
13. Hu, Y., et al., *Using indentation to characterize the poroelasticity of gels.* Appl Phys Lett, 2010. **96**(12): p. 121904-3.
14. Knapp, D.M., et al., *Rheology of reconstituted type I collagen gel in confined compression.* Journal of Rheology, 1997. **41**(5): p. 971-993.
15. Abazari, A., et al., *A Biomechanical Triphasic Approach to the Transport of Nondilute Solutions in Articular Cartilage.* Biophysical Journal, 2009. **97**(12): p. 3054-3064.
16. Lai, W.M., J.S. Hou, and V.C. Mow, *A Triphasic Theory for the Swelling and Deformation Behaviors of Articular Cartilage.* Journal of Biomechanical Engineering, 1991. **113**(3): p. 245-258.
17. Li, J., et al., *Self-assembled supramolecular hydrogels formed by biodegradable PEO-PHB-PEO triblock copolymers and [alpha]-cyclodextrin for controlled drug delivery.* Biomaterials, 2006. **27**(22): p. 4132-4140.
18. Sheu, M.-T., et al., *Characterization of collagen gel solutions and collagen matrices for cell culture.* Biomaterials, 2001. **22**(13): p. 1713-1719.
19. Okumura, Y. and K. Ito, *The Polyrotaxane Gel: A Topological Gel by Figure-of-Eight Cross-links.* Advanced Materials, 2001. **13**(7): p. 485-487.

20. Gong, J.P., et al., *Double-Network Hydrogels with Extremely High Mechanical Strength.* Advanced Materials, 2003. **15**(14): p. 1155-1158.
21. Zhang, S., et al., *Zuotin, a putative Z-DNA binding protein in Saccharomyces cerevisiae.* Embo J, 1992. **11**(10): p. 3787-96.
22. Zhang, S., et al., *Spontaneous assembly of a self-complementary oligopeptide to form a stable macroscopic membrane.* Proc Natl Acad Sci U S A, 1993. **90**(8): p. 3334-8.
23. Altman, M., et al., *Conformational behavior of ionic self-complementary peptides.* Protein Sci, 2000. **9**(6): p. 1095-105.
24. Zhang, S., *Emerging biological materials through molecular self-assembly.* Biotechnol Adv, 2002. **20**(5-6): p. 321-39.
25. Dai, J., *Characterization of self-assembling peptide nanofibers of KLD12 and RID12*, in *Department of Materials Science and Engineering*. 2004, Massachusetts Institute of Technology. p. 72.
26. Kisiday, J., et al., *Self-assembling peptide hydrogel fosters chondrocyte extracellular matrix production and cell division: implications for cartilage tissue repair.* Proc Natl Acad Sci U S A, 2002. **99**(15): p. 9996-10001.
27. Marini, D.M., et al., *Left-Handed Helical Ribbon Intermediates in the Self-Assembly of a ß-Sheet Peptide.* Nano Lett., 2002. **2**(4): p. 295-299.
28. Genove, E., et al., *The effect of functionalized self-assembling peptide scaffolds on human aortic endothelial cell function.* Biomaterials, 2005. **26**(16): p. 3341-51.
29. Brack, A. and L.E. Orgel, *Beta structures of alternating polypeptides and their possible prebiotic significance.* Nature, 1975. **256**(5516): p. 383-7.
30. Osterman, D.G. and E.T. Kaiser, *Design and characterization of peptides with amphiphilic beta-strand structures.* J Cell Biochem, 1985. **29**(2): p. 57-72.
31. Rippon, W.B., H.H. Chen, and A.G. Walton, *Spectroscopic characterization of poly(Glu-Ala).* 1973. **75**(2): p. 369.
32. Aggeli, A., et al., *Responsive gels formed by the spontaneous self-assembly of peptides into polymeric beta-sheet tapes.* Nature, 1997. **386**(6622): p. 259-62.
33. Collier, J.H., et al., *Thermally and photochemically triggered self-assembly of peptide hydrogels.* J Am Chem Soc, 2001. **123**(38): p. 9463-4.
34. Schneider, J.P., et al., *Responsive hydrogels from the intramolecular folding and self-assembly of a designed peptide.* J Am Chem Soc, 2002. **124**(50): p. 15030-7.
35. Zhang, S., et al., *Unusually stable beta-sheet formation in an ionic self-complementary oligopeptide.* Biopolymers, 1994. **34**(5): p. 663-72.
36. Aggeli, A., et al., *Hierarchical self-assembly of chiral rod-like molecules as a model for peptide beta -sheet tapes, ribbons, fibrils, and fibers.* Proc Natl Acad Sci U S A, 2001. **98**(21): p. 11857-62.
37. Caplan, M.R., et al., *Self-assembly of a beta-sheet protein governed by relief of electrostatic repulsion relative to van der Waals attraction.* Biomacromolecules, 2000. **1**(4): p. 627-31.
38. Haviv, L., et al., *Thickness distribution of actin bundles in vitro.* European Biophysics Journal, 2008. **37**(4): p. 447-454.
39. Caplan, M.R., et al., *Effects of systematic variation of amino acid sequence on the mechanical properties of a self-assembling, oligopeptide biomaterial.* J Biomater Sci Polym Ed, 2002. **13**(3): p. 225-36.

40. Sieminski, A.L., et al., *The stiffness of three-dimensional ionic self-assembling peptide gels affects the extent of capillary-like network formation.* Cell Biochem Biophys, 2007. **49**(2): p. 73-83.
41. Roeder, B.A., et al., *Tensile Mechanical Properties of Three-Dimensional Type I Collagen Extracellular Matrices With Varied Microstructure.* J. Biomech. Eng., 2002. **124**(2): p. 214-22.
42. Leon, E.J., et al., *Mechanical properties of a self-assembling oligopeptide matrix.* J Biomater Sci Polym Ed, 1998. **9**(3): p. 297-312.
43. Davis, M.E., et al., *Local myocardial insulin-like growth factor 1 (IGF-1) delivery with biotinylated peptide nanofibers improves cell therapy for myocardial infarction.* Proc Natl Acad Sci U S A, 2006. **103**(21): p. 8155-60.
44. Collier, J.H. and P.B. Messersmith, *Enzymatic modification of self-assembled peptide structures with tissue transglutaminase.* Bioconjug Chem, 2003. **14**(4): p. 748-55.
45. Haines, L.A., et al., *Light-activated hydrogel formation via the triggered folding and self-assembly of a designed peptide.* J Am Chem Soc, 2005. **127**(48): p. 17025-9.
46. Engler, A.J., et al., *Surface probe measurements of the elasticity of sectioned tissue, thin gels and polyelectrolyte multilayer films: Correlations between substrate stiffness and cell adhesion.* Surf Sci, 2004. **570**(1-2): p. 142-154.
47. Dimitriadis, E.K., et al., *Determination of Elastic Moduli of Thin Layers of Soft Material Using the Atomic Force Microscope.* Biophys J, 2002. **82**(5): p. 2798-2810.
48. Jacot, J.G., et al., *A simple microindentation technique for mapping the microscale compliance of soft hydrated materials and tissues.* J Biomed Mater Res A, 2006. **79A**(3): p. 485-494.
49. Lulevich, V., et al., *Cell Mechanics Using Atomic Force Microscopy-Based Single-Cell Compression.* Langmuir, 2006. **22**(19): p. 8151-8155.
50. Choi, Y., et al., *Size effects on the onset of plastic deformation during nanoindentation of thin films and patterned lines.* J Appl Phys, 2003. **94**(9): p. 6050-6058.
51. Buehler, M.J., *Nature designs tough collagen: explaining the nanostructure of collagen fibrils.* Proc Natl Acad Sci U S A, 2006. **103**(33): p. 12285-90.
52. Kennedy, H.J., A.C. Crawford, and R. Fettiplace, *Force generation by mammalian hair bundles supports a role in cochlear amplification.* Nature, 2005. **433**(7028): p. 880-3.
53. Mogilner, A. and B. Rubinstein, *The physics of filopodial protrusion.* Biophys J, 2005. **89**(2): p. 782-95.
54. Claessens, M.M., et al., *Actin-binding proteins sensitively mediate F-actin bundle stiffness.* Nat Mater, 2006. **5**(9): p. 748-53.
55. Kirschner, D.A., et al., *Synthetic peptide homologous to beta protein from Alzheimer disease forms amyloid-like fibrils in vitro.* Proc Natl Acad Sci U S A, 1987. **84**(19): p. 6953-7.
56. Aggeli, A., et al., *pH as a Trigger of Peptide β-Sheet Self-Assembly and Reversible Switching between Nematic and Isotropic Phases.* J Am Chem Soc, 2003. **125**(32): p. 9619-9628.

57. Benzinger, T.L., et al., *Two-dimensional structure of beta-amyloid(10-35) fibrils.* Biochemistry, 2000. **39**(12): p. 3491-9.
58. Balbach, J.J., et al., *Supramolecular structure in full-length Alzheimer's beta-amyloid fibrils: evidence for a parallel beta-sheet organization from solid-state nuclear magnetic resonance.* Biophys J, 2002. **83**(2): p. 1205-16.
59. Park, J., et al., *Atomistic simulation approach to a continuum description of self-assembled beta-sheet filaments.* Biophys J, 2006. **90**(7): p. 2510-24.
60. Holmes, T.C., et al., *Extensive neurite outgrowth and active synapse formation on self-assembling peptide scaffolds.* Proc Natl Acad Sci U S A, 2000. **97**(12): p. 6728-33.
61. Caplan, M.R., et al., *Control of self-assembling oligopeptide matrix formation through systematic variation of amino acid sequence.* Biomaterials, 2002. **23**(1): p. 219-27.
62. Hwang, W., et al., *Kinetic control of dimer structure formation in amyloid fibrillogenesis.* Proc Natl Acad Sci U S A, 2004. **101**(35): p. 12916-21.
63. Gordon, D.J., et al., *Increasing the amphiphilicity of an amyloidogenic peptide changes the beta-sheet structure in the fibrils from antiparallel to parallel.* Biophys J, 2004. **86**(1 Pt 1): p. 428-34.
64. Davis, M.E., et al., *Injectable self-assembling peptide nanofibers create intramyocardial microenvironments for endothelial cells.* Circulation, 2005. **111**(4): p. 442-50.
65. Narmoneva, D.A., et al., *Self-assembling short oligopeptides and the promotion of angiogenesis.* Biomaterials, 2005. **26**(23): p. 4837-46.
66. Semino, C.E., et al., *Entrapment of migrating hippocampal neural cells in three-dimensional peptide nanofiber scaffold.* Tissue Eng, 2004. **10**(3-4): p. 643-55.
67. Kisiday, J.D., et al., *Effects of dynamic compressive loading on chondrocyte biosynthesis in self-assembling peptide scaffolds.* J Biomech, 2004. **37**(5): p. 595-604.
68. Kim, G., *Characterization of a peptide biomaterial used for cell-seeded scaffolds with an analysis of relevant stem cell policy*, in *Department of Mechanical Engineering*. 2005, Massachusetts Institute of Technology.
69. Kis, A., et al., *Reinforcement of single-walled carbon nanotube bundles by intertube bridging.* Nat Mater, 2004. **3**(3): p. 153-7.
70. Brooks, B.R., et al., *CHARMM: A program for macromolecular energy, minimization, and dynamics calculations.* Journal of Computational Chemistry, 1983. **4**(2): p. 187-217.
71. Hoover, W.G., *Canonical dynamics: Equilibrium phase-space distributions.* Phys Rev A, 1985. **31**(3): p. 1695-1697.
72. Im, W., M.S. Lee, and C.L. Brooks, 3rd, *Generalized born model with a simple smoothing function.* J Comput Chem, 2003. **24**(14): p. 1691-702.
73. Feig, M., et al., *Performance comparison of generalized born and Poisson methods in the calculation of electrostatic solvation energies for protein structures.* J Comput Chem, 2004. **25**(2): p. 265-84.
74. Wong, S.E., K. Bernacki, and M. Jacobson, *Competition between intramolecular hydrogen bonds and solvation in phosphorylated peptides: simulations with explicit and implicit solvent.* J Phys Chem B, 2005. **109**(11): p. 5249-58.

75. Evans, E., D. Berk, and A. Leung, *Detachment of agglutinin-bonded red blood cells. I. Forces to rupture molecular-point attachments.* Biophys J, 1991. **59**(4): p. 838-48.
76. Evans, E. and K. Ritchie, *Dynamic strength of molecular adhesion bonds.* Biophys J, 1997. **72**(4): p. 1541-55.
77. Bathe, M., et al., *Cytoskeletal bundle mechanics.* Biophys J, 2007.
78. Evans, E., *Probing the relation between force--lifetime--and chemistry in single molecular bonds.* Annu Rev Biophys Biomol Struct, 2001. **30**: p. 105-28.
79. Doi, M. and S.F. Edwards, *The Theory of Polymer Dynamics.* 1986, New York: Oxford University Press.
80. Arkhipov, A., et al., *Coarse-grained molecular dynamics simulations of a rotating bacterial flagellum.* Biophys J, 2006. **91**(12): p. 4589-97.
81. Kis, A., et al., *Nanomechanics of microtubules.* Phys Rev Lett, 2002. **89**(24): p. 248101.
82. Salvetat, J.-P., et al., *Elastic and Shear Moduli of Single-Walled Carbon Nanotube Ropes.* Physical Review Letters, 1999. **82**(5): p. 944.
83. Satcher Jr, R.L. and C.F. Dewey Jr, *Theoretical estimates of mechanical properties of the endothelial cell cytoskeleton.* Biophysical Journal, 1996. **71**(1): p. 109-118.
84. Lu, K., et al., *Macroscale assembly of peptide nanotubes.* Chem Commun (Camb), 2007(26): p. 2729-31.
85. Drury, J.L. and D.J. Mooney, *Hydrogels for tissue engineering: scaffold design variables and applications.* Biomaterials, 2003. **24**(24): p. 4337-4351.
86. Khademhosseini, A. and R. Langer, *Microengineered hydrogels for tissue engineering.* Biomaterials, 2007. **28**(34): p. 5087-5092.
87. Drury, J.L., R.G. Dennis, and D.J. Mooney, *The tensile properties of alginate hydrogels.* Biomaterials, 2004. **25**(16): p. 3187-3199.
88. Mehta, G., et al., *Synergistic effects of tethered growth factors and adhesion ligands on DNA synthesis and function of primary hepatocytes cultured on soft synthetic hydrogels.* Biomaterials, 2010. **31**(17): p. 4657-4671.
89. Chau, Y., et al., *Incorporation of a matrix metalloproteinase-sensitive substrate into self-assembling peptides - A model for biofunctional scaffolds.* Biomaterials, 2008. **29**(11): p. 1713-1719.
90. Kopesky, P.W., et al., *Self-Assembling Peptide Hydrogels Modulate In Vitro Chondrogenesis of Bovine Bone Marrow Stromal Cells.* Tissue Eng Part A, 2009. **16**(2): p. 465-477.
91. Sun, J., et al., *Biocompatibility of KLD-12 peptide hydrogel as a scaffold in tissue engineering of intervertebral discs in rabbits.* J Huazhong Univ Sci Technolog Med Sci, 2010. **30**(2): p. 173-177.
92. Hutter, J.L. and J. Bechhoefer, *Calibration of atomic-force microscope tips.* Rev Sci Instrum, 1993. **64**(7): p. 1868-1873.
93. Sneddon, I.N., *The relation between load and penetration in the axisymmetric boussinesq problem for a punch of arbitrary profile.* Int J Eng Sci, 1965. **3**(1): p. 47-57.
94. Takigawa, T., et al., *Poisson's ratio of polyacrylamide (PAAm) gels.* Polymer Gels and Networks, 1996. **4**(1): p. 1-5.

95. Urayama, K., T. Takigawa, and T. Masuda, *Poisson's ratio of poly(vinyl alcohol) gels.* Macromolecules, 1993. **26**(12): p. 3092-3096.
96. Zhang, S., et al., *Design of nanostructured biological materials through self-assembly of peptides and proteins.* Curr Opin Chem Biol, 2002. **6**(6): p. 865-71.
97. Hwang, W., et al., *Supramolecular structure of helical ribbons self-assembled from a beta-sheet peptide.* J. Chem. Phys., 2003. **118**(1): p. 389-97.
98. Yokoi, H., T. Kinoshita, and S. Zhang, *Dynamic reassembly of peptide RADA16 nanofiber scaffold.* Proc Natl Acad Sci U S A, 2005. **102**(24): p. 8414-9.
99. Ye, Z., et al., *Temperature and pH effects on biophysical and morphological properties of self-assembling peptide RADA16-I.* J Pept Sci, 2008. **14**(2): p. 152-162.
100. Hammond, N.A. and R.D. Kamm, *Elastic deformation and failure in protein filament bundles: Atomistic simulations and coarse-grained modeling.* Biomaterials, 2008. **29**(21): p. 3152.
101. Knowles, T.P., et al., *Role of Intermolecular Forces in Defining Material Properties of Protein Nanofibrils.* Science, 2007. **318**(5858): p. 1900-1903.
102. Zhang, S., et al., *Self-complementary oligopeptide matrices support mammalian cell attachment.* Biomaterials, 1995. **16**(18): p. 1385-1393.
103. Hong, Y., et al., *Effect of Amino Acid Sequence and pH on Nanofiber Formation of Self-Assembling Peptides EAK16-II and EAK16-IV.* Biomacromolecules, 2003. **4**(5): p. 1433-1442.
104. Lamm, M.S., et al., *Laminated Morphology of Nontwisting β-Sheet Fibrils Constructed via Peptide Self-Assembly.* J Am Chem Soc, 2005. **127**(47): p. 16692-16700.
105. Kim, T., et al., *Computational analysis of viscoelastic properties of crosslinked actin networks.* PLoS Comput Biol, 2009. **5**(7): p. e1000439.
106. Flory, P.J., *Principles of polymer chemistry.* 1953, Ithaca: Cornell University Press.
107. Liu, J., et al., *Microrheology Probes Length Scale Dependent Rheology.* Phys Rev Lett, 2006. **96**(11): p. 118104.
108. Gelain, F., et al., *Designer Self-Assembling Peptide Nanofiber Scaffolds for Adult Mouse Neural Stem Cell 3-Dimensional Cultures.* PLoS ONE, 2006. **1**(1): p. e119.
109. Horii, A., et al., *Biological Designer Self-Assembling Peptide Nanofiber Scaffolds Significantly Enhance Osteoblast Proliferation, Differentiation and 3-D Migration.* PLoS ONE, 2007. **2**(2): p. e190.
110. Lutolf, M.P., et al., *Synthetic matrix metalloproteinase-sensitive hydrogels for the conduction of tissue regeneration: Engineering cell-invasion characteristics.* Proceedings of the National Academy of Sciences of the United States of America, 2003. **100**(9): p. 5413-5418.
111. Pelham, R.J. and Y.-l. Wang, *Cell locomotion and focal adhesions are regulated by substrate flexibility.* Proceedings of the National Academy of Sciences of the United States of America, 1997. **94**(25): p. 13661-13665.
112. Fassett, J., D. Tobolt, and L.K. Hansen, *Type I Collagen Structure Regulates Cell Morphology and EGF Signaling in Primary Rat Hepatocytes through cAMP-dependent Protein Kinase A.* Molecular Biology of the Cell, 2006. **17**(1): p. 345-356.

113. Keten, S., et al., *Nanomechanical Characterization of the Triple β -Helix Domain in the Cell Puncture Needle of Bacteriophage T4 Virus.* Cellular and Molecular Bioengineering, 2009. **2**(1): p. 66-74.